THE UNIVERSITY OF CALGARY

Robust Speed Control of a Reciprocating Compressor Driven by a Field Oriented Controlled Induction Motor

by

Wai Chi Alfred Chu

A THESIS

SUBMITTED TO THE FACULTY OF GRADUATE STUDIES

IN PARTIAL FULFILMENT OF THE REQUIREMENTS FOR THE

DEGREE OF MASTER OF SCIENCE

DEPARTMENT OF ELECTRICAL AND COMPUTER ENGINEERING

CALGARY, ALBERTA

December, 1998

National Library
of Canada

Acquisitions and
Bibliographic Services

395 Wellington Street
Ottawa ON K1A 0N4
Canada

Bibliothèque nationale
du Canada

Acquisitions et
services bibliographiques

395, rue Wellington
Ottawa ON K1A 0N4
Canada

Your file Votre référence

Our file Notre référence

0-612-38624-4

Canada

ABSTRACT

This thesis presents an application of robust control theories to control the speed of a reciprocating compressor driven by a field oriented controlled induction motor. The concepts and techniques of 'field orientation' are explained. A voltage source inverter driven field oriented controlled induction motor is implemented and tested to obtain an input-output model for robust speed controller design. The field oriented controlled induction motor loaded by a reciprocating compressor is considered as a plant whose speed should be robustly controlled. Relevant concepts in robust control are introduced. Feedback linearization is employed to reduce the size of the perturbed plant set and a controller is designed to achieve robust performance. The result indicates that under allowable test conditions, the system performs as designed. The work presented is thought to be useful for the natural gas industry for reducing polluting effluents in the process of natural gas compression.

ACKNOWLEDGMENTS

First I would like to thank my supervisor Dr. E. P. Nowicki and co-supervisor Dr. T. Chen for their constant support, advice and encouragement throughout the course of my study. They also proofread much of this thesis and made recommendations which helped me to better organize my thoughts.

Experiments performed in my research would have been impossible without the voltage source inverter built by D. Tardiff and the switching subroutine written by Dr. M. Mohammadian. The laboratory work was supported by Ed Evanik who helped and taught me a lot in practical matters on the implementation, debug and repair of circuits.

I also should thank a former colleague in Celestica Inc., Gunter Ladewig for his remarkable and insightful motto: "**All models are wrong**; although some could be useful", the power of which has been revealed everytime upon strange experimental results.

TABLE OF CONTENTS

LIST OF TABLES

LIST OF FIGURES

Figure Page

LIST OF ACRONYMS

Variable	Definition
BJT	Bipolar Junction Transistor
CSI	Current Source Inverter
DC link	the pair of bus bars across the legs of an inverter
DSP	Digital Signal Processor
FOC-IM	Field Oriented Controlled Induction Motor
LPF	Low Pass Filter
LTI	linear Time Invariant
MIMO	Multi-Input, Multi-Output
ODE	Ordinary Differential Equation
PFC	Power Factor Correction
QFT	Quantitative Feedback Theory
SISO	Single-Input, Single-Output
VSI	Voltage Source Inverter

LIST OF SYMBOLS

Symbol	Definition
$1(t)$	the unit step function
B	coefficient of friction
B_{motor}	coefficient of friction for motor bearings
i_A	phase A current
i_B	phase B current
i_C	phase C current
J	polar moment of inertia
J_{motor}	polar moment of inertia for motor(assumed constant)
K_t	torque constant for a field oriented controlled induction motor
p	complex variable used in Laplace transforms
T_e	electromagnetic torque generated
T_L	load torque
T_m	mechanical torque available for acceleration
T_{samp}	sampling period for field oriented control subroutine
U_{dc}	voltage across the DC link of a voltage source inverter
V/f	voltage over frequency, a technique of variable frequency control
ω_R	rotor speed
τ_S	stator time constant
τ'_S	stator subtransient time constant
τ_R	rotor time constant

Underlined variables : space vectors
superscript * : command variables
decoration $\hat{}$: estimated variables
decoration $\tilde{}$: perturbed variables

CHAPTER 1.

INTRODUCTION

1.1 Motivation

This thesis project was motivated by the desire to apply robust control theories to control the speed of a field oriented controlled induction motor (FOC-IM). Since a perfect FOC-IM has zero order dynamics from current to torque, it was thought that the project would be more challenging by coupling the FOC-IM to a reciprocating compressor.

1.2 Intended Application

Results from this project can be useful to the gas processing industry in which reciprocating gas compressors are driven by internal combustion engines. To eliminate pollutants from engine exhaust and flared gases, an alternative prime mover is a robustly controlled FOC-IM that provides variable speed operation. A more detailed discussion on the benefits and feasibility of this alternative can be found in Appendix A.

1.3 Contributions of Thesis

Contributions in FOC-IM The heralded work of Leonhard [L1] provides this thesis with the theoretical foundation of FOC-IM. The mechanical analogy and the principles of FOC-IM presented in chapter 2 are inspired by this major reference. In the implementation of a feedforward decoupled, indirect FOC-IM driven by a voltage source inverter (VSI), the comprehensive work of Vas [V1] has been an invaluable source. This thesis contributes in the area of FOC-IM in the following ways.

- Explored and extended the mechanical analogy presented in [L1] for improved visualization of the operating principles related to field oriented control.

- Provided a thorough derivation for the voltage decoupling terms for a VSI-driven FOC-IM. The derivation augments the intuitive explanations offered in both [L1] and [V1].

- Discovered by simulation the peculiar nature of torque transients of a detuned VSI driven FOC-IM. In short, when the resistance parameters in the model are set greater than the actual values, the electromagnetic torque would oscillate. The off line tuning procedure for a VSI driven FOC-IM is therefore very different from that of a CSI driven one. Furthermore, the simulations revealed that under certain detuned conditions, the input-output behavior of a VSI-driven FOC-IM may still be considered as a linear time invariant (LTI) plant.

- Discovered the speed variant saturation limits of a VSI driven FOC-IM caused by the voltage decoupling terms. This discovery contributes to the knowledge required for designing an effective and efficient VSI driven FOC-IM. This is because a linear control system with controller output exceeding the hardware limit will simply not function according to the designed control law. For efficient use of equipment, saturations can be dealt with by non-linear techniques such as clamping of integrating actions or more elegantly, saturation feedback[1].

Contributions in Robust Control In this thesis, the basics of modelling with multiplicative uncertainties, designing with the loop shaping technique and verifications using the robust performance criterion are adopted from the famous work of Doyle, Francis and Tannenbaum[D1]. Considerable insights on how to treat uncertainties had been provided by [D1] and Zhou in his recent book[Z1]. For most plant models, uncertainties are usually minimal in the low frequency region on the magnitude plot. For such models, the choice of the nominal plant and subsequently the application of the loop shaping technique are well covered in literatures. It has been pointed out in [D1] that when substantial uncertainties exist in the model, the task of satisfying the robust performance criterion with loop shaping would become more difficult. It turned out that this difficult situation is the case for this project. The difficulties were overcome by a technique discussed in Chapter 3. The contribution to robust control by this thesis is humbly as follow.

- For multiplicative uncertain models with substantial low frequency uncertainties, the task of loop shaping would be easier when the nominal model is chosen as the upper bound of the set of perturbed models. This technique is suitable for applying robust control to a general class of problems encountered in classical control[2].

---

[1] Saturation feedback is a non-linear technique for handling saturation problems. One such technique that deals with constant limits can be found in [M2]. However, it is not known to the author if a technique exists that addresses varying saturation limits.

[2] From the view points of classical control, an uncertain model with substantial low frequency uncertainties is often treated as a plant with a varying operating point. An interesting example is

Contributions in Robust Speed Control of an FOC-IM There is much in the literature on robust control, and separately much on FOC-IM. While research on robust control has mostly been done in the abstractions of rigorous mathematics, there are many other issues beside control theory that must be solved in building an FOC-IM. As a result, there exist only a few research papers ([L3], [L5] and [T2]) on the design of a robust speed controller for an FOC-IM. Among these few papers, only [T2] addresses modelling uncertainties explicitly. The technique of accommodating the neglected and unknown dynamics in [T2] is adopted in this thesis. This thesis project is different from [L3], [L5] and [T2] in the follower manner.

- Certain characteristics of the load (a reciprocating compressor) are incorporated in the modelling process. It is believed that by doing so, the resulting system will be more efficient than one that assumes a random load disturbance.
- Feedback linearization is employed to modify the plant for reducing the size of the set of perturbed models.
- While [T2] achieves robust performance by augmenting an optimal internal model controlled system with a robust compensator, this thesis project attempts to obtain a robust design directly by loop shaping.

Contributions to Laboratory Work The VSI available for this project was built by D. Tardiff ([T1]). The interfacing hardware were primarily designed and built by M.

---

the current loop of a boost derived power factor correction (PFC) circuit. For this PFC circuit, the control voltage to a comparator and the inductor current are treated as the input and output respectively, while the 120 Hz rectified sinusoidal supply voltage is viewed as a varying operating point.

Mohamadian and E. Evanik. The communication (between user and microprocessor), data acquisition and VSI switching subroutines were primarily designed by M. Mohamadian. The author contributes to the hardware and software in the following manner.

- Retraced the interfacing circuits built on bread boards and rebuilt the hardware on vector boards.
- Modified the communication routines to acquire data more efficiently, and accept a wider variety of asynchronous commands.
- Constructed and modified auxiliary equipment for connecting a reciprocating compressor to the FOC-IM.
- Installed a new speed encoder and current sensors; modified the hardware and software accordingly.
- Rewrote the field oriented control and speed control subroutines according to the work presented in this thesis.

1.4 Objective and Layout of Thesis

Objective The objective of this thesis is to design and implement a robust speed controller for a VSI powered FOC-IM that drives a reciprocating compressor.

Limitations Due to a lack of a suitable pressure sensor and associated equipment, the compressor is arranged to discharge against atmospheric pressure. It is believed that a subsequent design of a regulatory pressure loop can be performed without knowing the inner details of the speed loop.

Layout of Thesis This thesis is organized in 6 chapters and 6 appendices. Except for chapter 1, each chapter is furnished with a discussion section and a summary section. The discussion sections contain various opinions of the author that are relevant to the chapters. Chapters are organized as follows.

- Chapter 1 describes the motivations, contributions, objectives and limitations of this thesis.
- Chapter 2 presents relevant principles and equations of the indirect VSI driven FOC-IM.
- Chapter 3 presents the details involved in the implementation of the indirect VSI driven FOC-IM.
- Chapter 4 presents relevant principles and equations in robust control theories.
- Chapter 5 presents the details and results in the design and implementation of the robust speed controlled VSI driven FOC-IM for a reciprocating compressor.
- Chapter 6 provides conclusions and recommendations for future work.

CHAPTER 2.

INTRODUCTION TO INDIRECT FOC-IM

2.1 Literature Reviews

Rapid torque control of an induction motor has been the concern of researchers for several decades. The key is to control the torque and flux producing current components separately. The challenge is in obtaining the flux signal accurately. In 1971, Blaschke proposed and verified the concept of the so called direct FOC-IM[B1] using flux sensors. However, the incorporation of a flux sensor is an undesirable feature. In 1977, Abbondanti presented a flux estimation method using phasor analysis [A1] and initiated the trend of indirect field oriented control. The space vector model for field oriented control adopted in this section was published in 1979 by Gabriel, Leonhard and Norby [G1]. The same results can also be arrived at by employing the two axis theory presented in [K1]. Since its invention, the space vector model has provided foundations for most implementations of FOC-IM including speed sensorless drives. A comprehensive review of indirect FOC-IM can be found in [V1]. As stated in a recent (1994) summary of the status of induction motor control by Lorenz, Lipo and Novotny[L2]: "...by the early 1980's the details of the control concept had been almost completely resolved". From the mid 1980's to the mid 1990's, the research efforts on indirect field oriented control were focused on harnessing various non-ideal effects that are not incorporated in the space vector model. Most of the research work was related to the identification and automatic tuning of motor parameters [K2][W2][M1]. The extensive contributions in identification also lead to the beginning of investigations in speed sensorless FOC-IM which remains an active research subject.

2.2 A Mechanical Analogy

In Figure 2..1, a mechanical system is presented to aid in the visualization of field orientation principles[1].

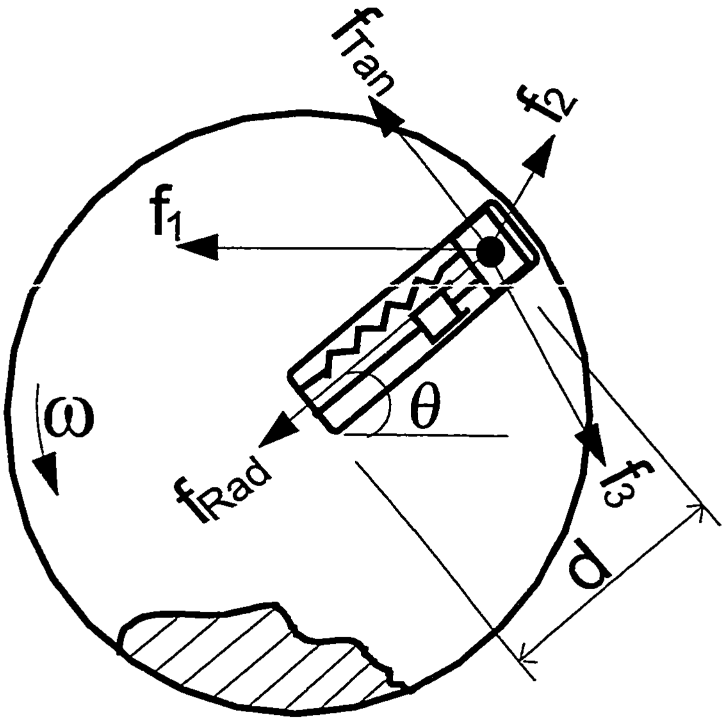

Figure 2..1: A mechancial analogy to field orientation

A disc pivoted at its centre is rotated by the combined efforts of the forces f_1, f_2 and f_3 acting on a swivel pin. These forces are analogous to the electromagnetic

---

[1] The mechanical disc system shown in Figure (2..1) is inspired by a similar diagram presented in the famous work of Leonhard [L1]. The observations drawn from the diagram and the comparison are contributed by the author of this thesis.

forces produced by the windings of a three phase motor. The directions of these forces are defined and restrained in a stationary frame. The swivel pin, at a distance d from the center and angle θ from a stationary reference axis, is allowed to slide against a spring and damper inside a slot on the disc. This distance d is analogous to the magnitude of rotor flux in an induction motor. The angular speed of the disc is represented by ω.

To rotate the disc effectively, the three forces must be coordinated in their magnitudes at every instance. The worst coordination would lead to compression and relaxation of the spring without a torque applying to the disc. The control problem can be phrased as follows. Given ω, d and θ as observable variables, calculate the magnitudes of the forces required to track a speed command. The key to the solution is to focus on how the torque is created for accelerating (or decelerating) the disc. At the swivel pin, the three forces can be resolved, with respect to coordinates fixed on the rotating disc, into a tangential component, f_{Tan} and a radial component f_{Rad}. The following observations are noteworthy.

- Assuming the masses of the spring, damper and the sliding block are all negligible, the distance d is affected only by f_{Rad} in the form of a first order ordinary differential equation (ODE). For the control of d, a linear controller can be designed using f_{Rad} as the actuator signal.

- The generated torque T_m is equal to $f_{Tan} \times d$. Since an instantaneous step change in d is not possible, fast torque control can only be achieved through the control of f_{Tan}.

- If d is maintained constant by a suitable f_{Rad}, the torque produced is linearly proportioned to f_{Tan}. **A torque command T_m^* can be satisfied "instantaneously" by a correctly proportioned f_{Tan}.**
- From the history of ω, θ can be found. Given f_{Tan}, d and θ, the required magnitudes of f_1, f_2 and f_3 to achieve T_m^* can be calculated.

As will be shown later, the algorithm for field oriented control is to decompose current vectors along suitable axes for decoupling the control of torque and flux. The underlying concept is similar to the observations listed above.

2.3 Space Vector Model for a Three Phase Squirrel Cage Motor

Field oriented control can be conveniently explained in terms of space vectors (see Appendix B). Various space vector variables are shown [L1] to be related to each other shown in the following familiar equations:

$$\underline{\psi}_S = L_S \underline{i}_S + L_o \underline{i}_R e^{j\varepsilon} \tag{2..1}$$

$$\underline{\psi}_R = L_R \underline{i}_R + L_o \underline{i}_S e^{-j\varepsilon} \tag{2..2}$$

$$\underline{u}_S = R_S \underline{i}_S + \frac{d\underline{\psi}_S}{dt} \tag{2..3}$$

$$\underline{u}_R = R_R \underline{i}_R + \frac{d\underline{\psi}_R}{dt} \tag{2..4}$$

where

- underlined variables are space vectors.

- subscript $_S$ denotes reference to the stator frame and $_R$ to the rotor frame.

- $\underline{\psi}$, $\underline{i}$, and $\underline{u}$ are the *time variant* flux linkage, current and voltage space vector variables respectively.

- L, L_o and R are constants, representing self inductance, mutual inductance and resistance respectively.

- ε is the angle between the reference axes of the stator and the rotor frame.

It is also shown in [L1] that

$$T_e = \left(\frac{P}{2}\right)\left(\frac{2}{3}\right) L_o \,\mathrm{Im}[\underline{i}_S(\underline{i}_R e^{j\varepsilon})^{conj}] \qquad (2..5)$$

where

- T_e is the electromagnetic torque generated by the three phase squirrel cage motor.

- P is the number of poles.

From 2..1, 2..2, 2..3 and 2..4, it is straightforward to prove the following.

$$\underline{u}_S = R_S\underline{i}_S + L_S\frac{d\underline{i}_S}{dt} + L_o\frac{d\underline{i}_R}{dt}e^{j\varepsilon} + j\omega L_o\underline{i}_R e^{j\varepsilon} \quad \omega = \frac{d\varepsilon}{dt} \qquad (2..6)$$

$$\underline{u}_R = 0 = R_R\underline{i}_R + L_R\frac{d\underline{i}_R}{dt} + L_o\frac{d\underline{i}_S}{dt}e^{-j\varepsilon} + j\omega L_o\underline{i}_R e^{-j\varepsilon} \qquad (2..7)$$

Equations 2..5, 2..6 and 2..7 constitute the space vector model of a polyphase squirrel cage motor, as well as the starting point for deriving the conditions required for decoupling the torque and flux producing currents.

2.4 Field Orientation of the Stator Current Vector

For a squirrel cage motor, variables in the rotating frame are not directly accessible. It is therefore desirable to express the model in terms of variables defined in the stator frame. It turns out that an equivalent rotor flux magnetizing current vector $\underline{i}_m$ defined in the stator frame is an appropriate variable. Let $\underline{i}_m = i_m e^{j\rho}$, where ρ is the angular position of the rotor flux space vector referenced to the stator frame. The following equation states that when $\underline{\psi}_R$ is viewed from the stator frame, it can be thought of as being produced by the current $\underline{i}_m$.

$$[L_R \underline{i}_R + L_o \underline{i}_S e^{-j\varepsilon}]e^{j\varepsilon} = \underline{\psi}_R e^{j\varepsilon} = L_o \underline{i}_m \tag{2..8}$$

Equivalently,

$$\underline{i}_R e^{j\varepsilon} = [\underline{i}_m - \underline{i}_S]/(1 + \sigma_R) \tag{2..9}$$

where σ_R is the rotor leakage factor and $L_R = (1 + \sigma_R)L_o$.

Equations (2..5) and (2..9) lead to what is known as **"field orientation" of the stator current in the rotor flux frame:**

$$T_e = K_e i_m IM[\underline{i}_S e^{-j\rho}] \qquad K_e = \left(\frac{P}{2}\right)\left(\frac{2}{3}\right) L_o/(1 + \sigma_R)$$

The value of $IM[\underline{i}_S e^{-j\rho}]$ can be obtained as the projection of the vector $\underline{i}_S e^{-j\rho}$ on the imaginary axis of the stator frame. Alternatively, consider a dq frame whose d axis aligns with $\underline{i}_m$ at all times and the q axis 90° away from the d axis; and let this dq frame be known as the *rotor flux frame*. The value of $IM[\underline{i}_S e^{-j\rho}]$ can also be obtained as the projection of $\underline{i}_S$ onto the q axis of the rotor flux frame. In fact, $\underline{i}_S e^{-j\rho}$ should be interpreted as $\underline{i}_S$ being observed in the rotor flux frame. Hence the name field orientation.

In terms of the d and q components in the rotor flux frame,

$$\underline{i}_S e^{-j\rho} = i_{Sd} + j i_{Sq} \tag{2..10}$$

A geometric representation of Equation (2..10) is shown in Figure 2..2. Notice that when ρ is known and the line currents can be manipulated freely, $\underline{i}_S$ and hence any combinations of i_{Sd} and i_{Sq} can be realized for controlling the motor.

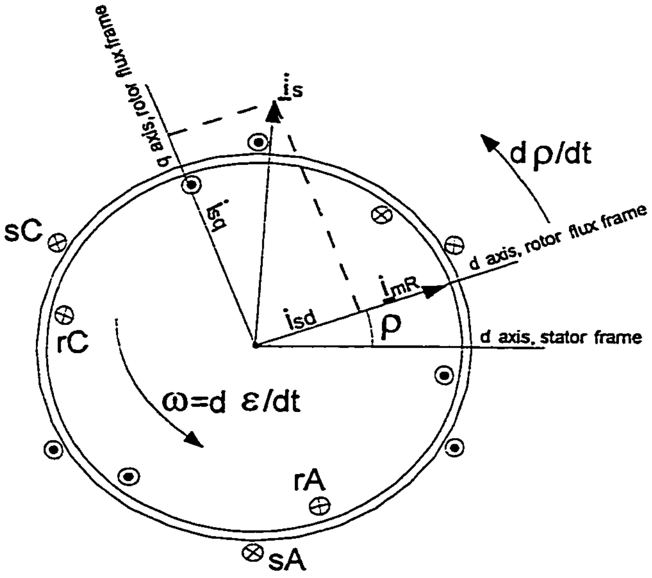

Figure 2..2: Field oriented components of $\underline{i}_S$

Significance of i_{Sq} With $IM[\underline{i}_S e^{-j\rho}] = i_{Sq}$, the torque equation can be written as

$$T_e = K_e i_m i_{Sq} \tag{2..11}$$

Thus **the electromagnetic torque T_e responds instantaneously to the torque producing current i_{Sq}.** Of course, T_e is also instantaneously controllable with respect to i_m which is only accessible through i_{Sd} (described below).

Significance of i_{Sd} Rewriting Equation (2..4) in terms of $\underline{i}_m$ and $\underline{i}_S$, the following first order vector differential equation is obtained.

$$\tau_R \frac{d}{dt}[\underline{i}_m e^{-j\varepsilon}] + \underline{i}_m(t) e^{-j\varepsilon} = \underline{i}_S e^{-j\varepsilon} \qquad \tau_R = L_R/R_R \tag{2..12}$$

where τ_R is also known as the rotor time constant. Differentiating Equation (2..12), and separating the results into real and imaginary parts, two scalar equations are obtained.

$$\tau_R \frac{di_m}{dt} + i_m = i_{Sd} \tag{2..13}$$

$$\rho = \int_0^t \frac{i_{Sq}}{\tau_R i_m} dt + \varepsilon \qquad \varepsilon(0) = 0 \qquad \rho(0) = 0 \tag{2..14}$$

Equation (2..13) shows that **the magnetizing current i_m is governed by i_{Sd}** through time constant τ_R. The integrand in Equation (2..14) is known as the slip speed. For discrete time implementation, $\rho[k]$ can be calculated approximately from $\rho[k-1]$, $\underline{i}_{Sq}[k-1]$, $i_m[k-1]$ and $\varepsilon[k-1]$.

Torque control under ideal conditions For fast torque control, i_m can be regulated by a constant command i^*_{Sd}. Assuming $i_m = i^*_{Sd}$ after an initial start up time, a torque command can be realized instantaneously by a corresponding i^*_{Sq} according to Equation (2..11). The knowledge of i^*_{Sd}, i^*_{Sq} and ρ allows the calculation of phase currents to be injected in the power lines. For CSI driven motors, the similarities between the indirect FOC-IM and the rotating mechanical disc shown in Figure 2..1 are becoming clear. The key variables in the two systems are analogous to each other as indicated in Table 2.1.

Table 2.1: Comparison of variables for analogous systems

Head	**FOC-IM**	**Rotating Disc**	Reference Frame
Phase Variables	i_{SA}, i_{SB}, i_{SC}	f_1, f_2, f_3	Stationary
Vector Sum	$\underline{i}_S$	$\underline{f}$	Stationary
Moment Arm	i_m	d	
Angular Position	ρ	θ	Stationary
Moment Arm Control Signal	i_{Sd}	f_{Rad}	Rotating
Torque Control Signal	i_{Sq}	f_{Tan}	Rotating
Torque	$K_e i_m i_{Sq}$	$K_m d f_{Tan}$	

2.5 Voltage Source Inverter

Although the principles of indirect FOC-IM can be clearly explained in terms of a CSI driven motor, inverters constructed with BJT's are often voltage sources rather than current sources. Several complications are involved for achieving field oriented control with a VSI driven motor. A typical arrangement of power components for a VSI is shown in Figure 2..3.

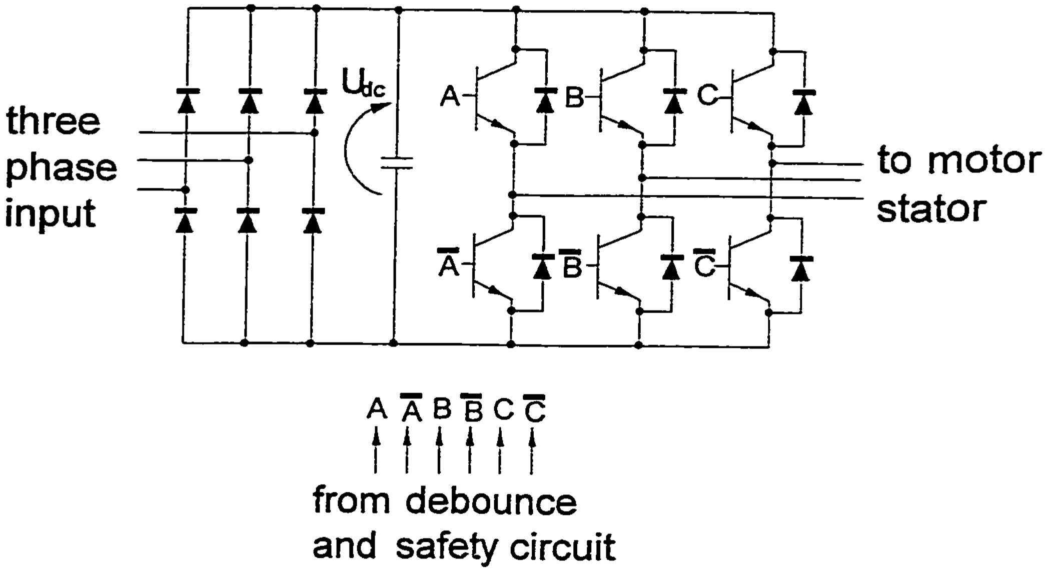

Figure 2..3: A voltage source inverter

Operating Principles Referring to Figure 2..3, a three phase voltage is rectified and filtered to provide a voltage U_{dc} across three branches of transistor switches. For obvious reasons, U_{dc} is known as the *DC link voltage*. Power to the induction motor is conveyed by the three lines tapped from the middle of each the three branches of switches (or *inverter legs*). For each branch, complementary Boolean signals X and $\overline{X}$ ($X = A$, B or C) are applied to the switches to prevent a short across the DC link. To accommodate durations required for a switch to become fully on or fully off, a safety circuit can be used to ensure that X is completely off before switching on $\overline{X}$ and vice versa. The triplet $[A, B, C]$ is known as the switch vector. The switch vector can assume any one of the eight states as shown in Table 2.2 (L represents a Low gate voltage and H represents a High gate voltage).

Depending on the state of the switch vector, the windings in the motor are

Table 2.2: Inverter switch combinations and vector representation

state	switch A	switch B	switch C	stator voltage vector $\underline{u}_S$
0	L	L	L	$\underline{u}_0$
1	H	L	L	$\underline{u}_1$
2	H	H	L	$\underline{u}_2$
3	L	H	L	$\underline{u}_3$
4	L	H	H	$\underline{u}_4$
5	L	L	H	$\underline{u}_5$
6	H	L	H	$\underline{u}_6$
7	H	H	H	$\underline{u}_7$

energized to realize the stator voltage vector $\underline{u}_S$ in one of the seven unique states shown in Figure 2..4. Note that for the motor, the effect of $[A, B, C] = [L, L, L]$ or $[H, H, H]$ is the same in that all line to line voltages are zero, *i.e.* $u_0 = u_7 = 0$. From states 1 to 6 (correspond to the vectors $\underline{u}_1$, $\underline{u}_2 ... \underline{u}_6$), the magnitude of the stator voltage vector is $u_S = U_{dc}$ and $\theta = 0^o, 60^o, ...300^o$ respectively.

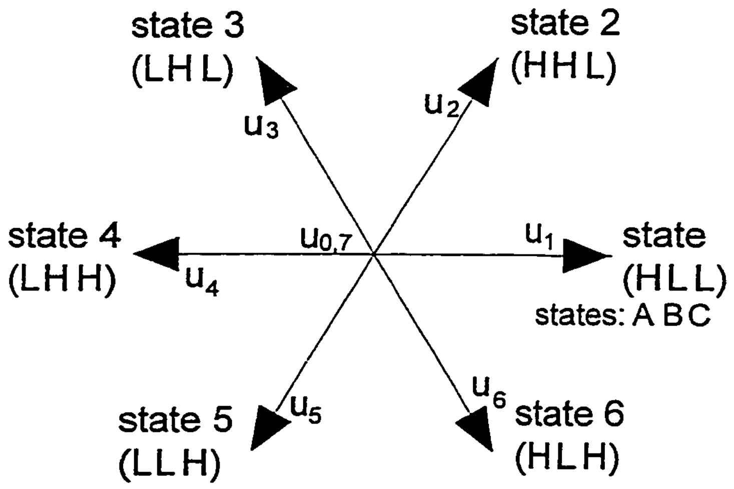

Figure 2..4: The eight states of an inverter

To realize an average voltage space vector within a time interval, the inverter can be switched back and forth between two adjacent states. As an example, Figure

2..5 shows how an arbitrary command $\underline{u}_S^* = u_S e^{j\theta}, 0^o < \theta < 60^o$ can be constructed geometrically from $\underline{u}_1$ and $\underline{u}_2$.

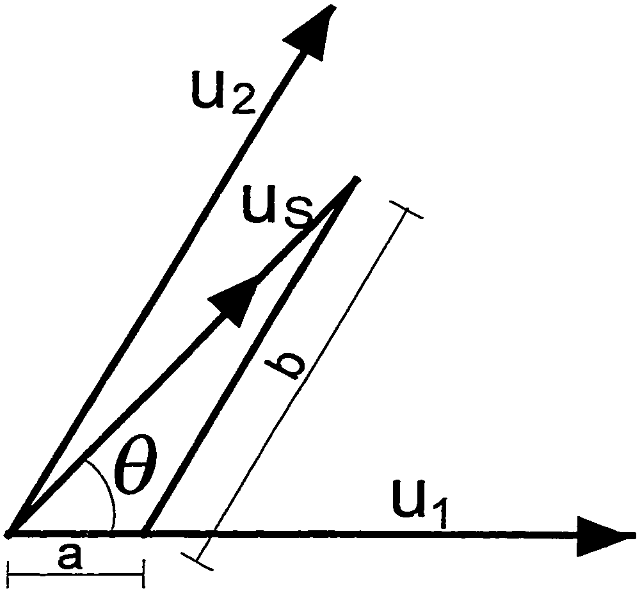

Figure 2..5: Realizing $\underline{u}_S$ by switching between states

For a switch period T_{sw},

$$T_{sw}\underline{u}_S = xT_{sw}\underline{u}_0 + aT_{sw}\underline{u}_1 + bT_{sw}\underline{u}_2 + yT_{sw}\underline{u}_7 \tag{2..15}$$

where $a + b < 1$, $x \leq (1 - a - b)$ and $y \leq (1 - x)(1 - a - b)$. Equation (2..15) implies that the overall effect of $\underline{u}_S$ for an interval of T_{sw} can be approximated by the sequence $[\underline{u}_0, \underline{u}_1, \underline{u}_2, \underline{u}_7]$ with corresponding durations $[x, a, b, y]T_{sw} \triangleq [t_0, t_1, t_2, t_3]$. Notice that the state sequence starts and ends with zero voltages; and each change of state requires a change of only a single element in the switch vector. The corresponding timing diagram is shown in Figure 2..6. In the figure, U_{SA}, U_{SB} and U_{SC} are the instantaneous phase voltage magnitudes.

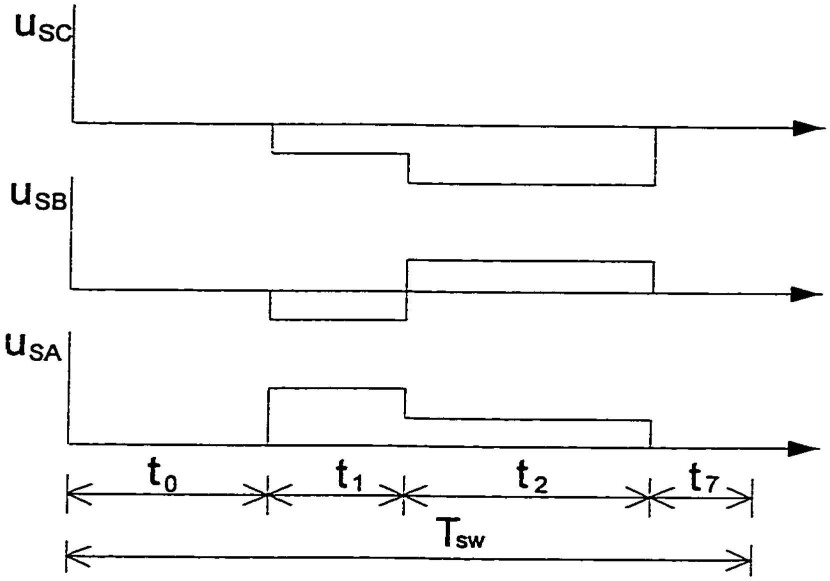

Figure 2..6: Timing diagram for one switching period

2.6 Feedforward Decoupling for a *VSI* Driven FOC-IM

For a motor driven by a voltage source inverter (VSI) operating at a frequency below 15 kHz, the current command values cannot be achieved "instantaneously". The stator voltage equation, Equation (2..6), must be taken into account for achieving decoupling control of torque and flux. Introducing the overall leakage factor

$$\sigma = 1 - \frac{1}{(1+\sigma_S)(1+\sigma_R)}$$

and substituting $\underline{i}_R e^{j\epsilon}$ from Equation (2..9), Equation (2..6) becomes

$$\begin{aligned} \underline{u}_S &= R_S \underline{i}_S + \sigma L_S \frac{d[(\underline{i}_S e^{-j\rho}) e^{j\rho}]}{dt} + (1-\sigma) L_S \frac{d(i_m e^{j\rho})}{dt} \\ &= R_S \underline{i}_S + \sigma L_S \frac{d[(i_{Sd} + j i_{Sq}) e^{j\rho}]}{dt} + (1-\sigma) L_S \frac{d(i_m e^{j\rho})}{dt} \end{aligned}$$

The above equation can be multiplied on both sides by $e^{-j\rho}$ and differentiated. Furthermore, realizing that $\underline{u}_S e^{-j\rho} = u_{sd} + j u_{sq}$ in the rotor flux frame (Chapter 2, Section

4), the real and imaginary components of the differentiated result can be separated to form the following two scalar equations:

$$\tau'_S \frac{di_{Sd}}{dt} + i_{Sd} = \frac{u_{Sd}}{R_S} + \tau'_S \omega_m i_{Sq} - (\tau_S - \tau'_S) \frac{di_m}{dt} \tag{2..16}$$

$$\tau'_S \frac{di_{Sq}}{dt} + i_{Sq} = \frac{u_{sq}}{R_S} - \omega_m \tau'_S i_{Sd} - (\tau_S - \tau'_S) \omega_m i_m \tag{2..17}$$

where $\tau'_S = \sigma L_S / R_S$ and $\omega_m = d\rho/dt$. **Equations (2..16), (2..17) together with (2..11), (2..13) and (2..14) form the mathematical model of a VSI driven FOC-IM.** From Equations (2..16) and (2..17), it is clear that the i_{Sd} and i_{Sq} are coupled to each other when the motor is fed by a VSI. To achieve independent control of i_{Sd} and i_{Sq}, decoupling circuits are needed.

From Equation (2..13), $di_m/dt = (i_{Sd} - i_m)/\tau_R$. With τ_R relatively large and command value i^*_{Sd} kept constant, it is practical to assume $di_m/dt \cong 0$, $i_m = i_{Sd}$ after an initial start-up period. For zero dynamics from $[u^*_{Sd}, u^*_{Sq}]$ to $[u_{Sd}, u_{Sq}]$, Equations (2..16) and (2..17) can be rewritten as

$$\tau'_S \frac{di_{Sd}}{dt} + i_{Sd} = i^*_{Sd} + \tau'_S \omega_m i_{Sq}, \qquad i^*_{Sd} = u^*_{Sd}/R_S \tag{2..18}$$

$$\tau'_S \frac{di_{Sq}}{dt} + i_{Sq} = i^*_{Sq} - \tau_S \omega_m i_{Sd}, \qquad i^*_{Sd} = u^*_{Sd}/R_S \tag{2..19}$$

Graphically, Equations (2..18) and (2..19) can be represented as a cross coupled plant in Figure 2..7a with the transfer characteristics $G_1 = G_2 = 1/(\tau'_S p + 1)$, $H_1 = -\tau_S \omega_m$ and $H_2 = \tau'_S \omega_m$.

A simple decoupling method is to use feedforward terms derived from command values. In Figure 2..7b, the decoupling terms d_1 and d_2 are injected into the input.

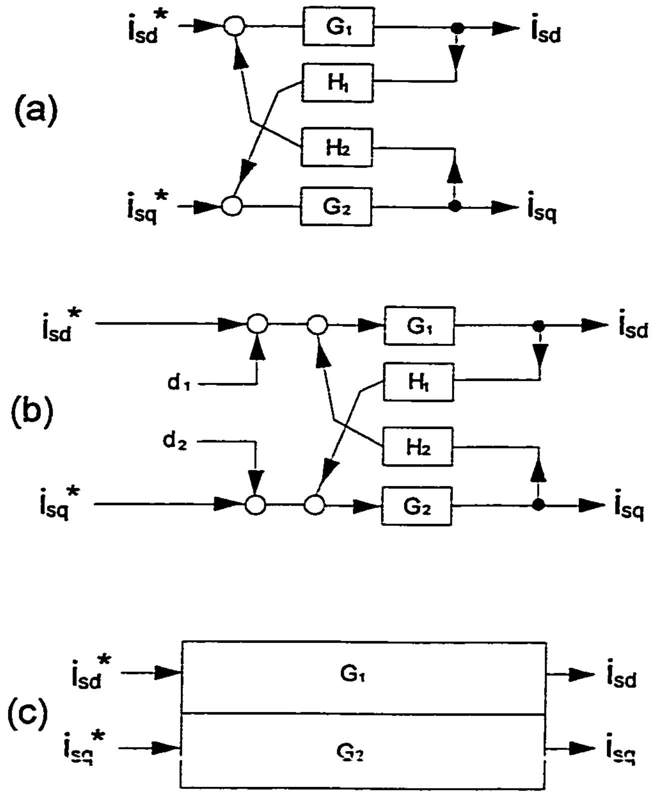

Figure 2..7: Decoupling a cross coupled plant

The output would be

$$\begin{bmatrix} i_{sd} \\ i_{sq} \end{bmatrix} = A^{-1}B \begin{bmatrix} i^*_{Sd} + d_1 \\ i^*_{Sq} + d2 \end{bmatrix}$$

where

$$A = \begin{bmatrix} 1 & -G_1H_2 \\ G_2H_1 & 1 \end{bmatrix}$$

$$B = \begin{bmatrix} G_1 & 0 \\ 0 & G_2 \end{bmatrix}$$

If appropriate decoupling terms exist, the output should be equal to

$$B \begin{bmatrix} i^*_{Sd} \\ i^*_{Sq} \end{bmatrix}$$

That is,

$$B \begin{bmatrix} i^*_{Sd} \\ i^*_{Sq} \end{bmatrix} = A^{-1} B \begin{bmatrix} i^*_{Sd} + d_1 \\ i^*_{Sq} + d2 \end{bmatrix}$$

which yields

$$\begin{bmatrix} d_1 \\ d_2 \end{bmatrix} = \begin{bmatrix} 0 & -G_2 H_2 \\ -G_1 H_1 & 0 \end{bmatrix} \begin{bmatrix} i^*_{Sd} \\ i^*_{Sq} \end{bmatrix}$$

With $\tau'_S << 1$, $G1 = G2 \cong 1$. Therefore, the decoupling terms can be approximated by

$$d_1 \cong -\tau'_S \omega_m i^*_{Sq} \qquad d_2 \cong \tau_S \omega_m i^*_{Sd} \tag{2..20}$$

The effects of injecting d_1 and d_2 in Figure 2..7b would result in a plant close to Figure 2..7c. That is, the command to output transfer functions can be approximated by

$$tf : i^*_{Sd} \mapsto i_{Sd} = 1/(\tau'_S p + 1) \tag{2..21}$$

$$tf : i^*_{Sq} \mapsto i_{Sq} = 1/(\tau'_S p + 1) \tag{2..22}$$

The feedforward decoupling operation with its inputs and outputs can be realized as shown in Figure 2..8.

2.7 Discussion

Impact of Switch Mode Operation on Current Measurements When a current vector is implemented by an inverter with a fixed sampling period T_{samp}; there are three

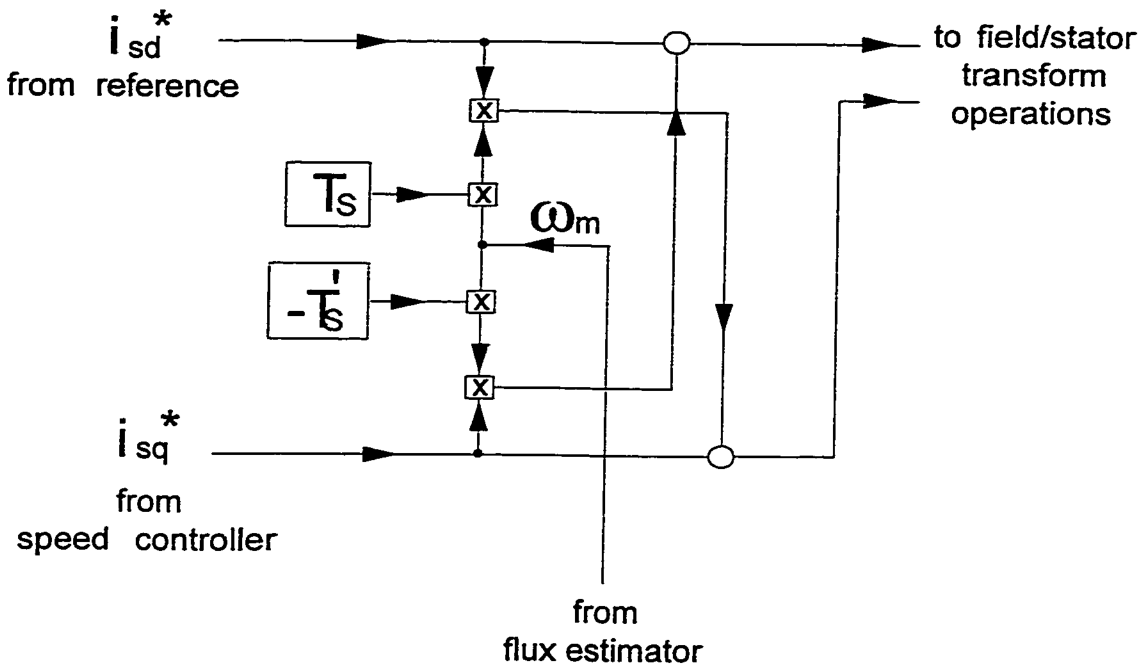

Figure 2..8: Realization of feedforward decoupling

changes of the inverter state within T_{samp}(assuming switching and sampling periods are equal). The line currents are usually sampled at the beginning of T_{samp} when the inverter is at state 0. Since i_m and i_{Sd} are commanded to stay constant and related by a first order ODE with a relatively large time constant, it is expected that for a small T_{samp} the line currents will contain the full information of i_m or i_{Sd}. The same cannot be said for i_{Sq} which may vary in a wide range and associated with a much smaller time constant. In fact, when the inverter is switched back to the zero state and line currents are measured, it is difficult to determine how much the line current samples are 'contaminated' by i_{Sq}. Rather than introducing problems with doubtful benefits in using feedback, it is decided that a feedforward scheme should be used to estimate i_{Sd} and i_{Sq}.

2.8 Summary

A mechanical analogy intended to provide insights into the operating principles of an indirect FOC-IM is presented (section 2). Field orientation in general builds on a dynamic model of the motor and aims to achieve independent control of torque and flux. The essence of a so called space vector model published in [L1] is presented (section 3) for explaining the mechanisms of a CSI driven FOC-IM (section 4). Although field orientation can best be explained using a CSI drive model, the available inverter for this project is a VSI. The operating principles of a VSI are therefore introduced (section 5). To achieve independent control of torque and flux for a VSI driven FOC-IM, simple feedforward voltage decoupling terms are derived (section 6). A question on the accuracy of estimating the flux magnitude and position from line currents is discussed (section 7). It is decided that feedback control of currents should be avoided in this project.

CHAPTER 3.

IMPLEMENTATION OF THE FIELD ORIENTATION CONTROLLER

This chapter discusses various aspects in the implementation of the indirect FOC-IM. The focus of implementation is to obtain the allowable signal limits, and the input-output description of the VSI driven FOC-IM suitable for the design of a robust speed controller.

3.1 System Operation

A block diagram illustrating hardware and software implementation of an indirect FOC-IM is shown in Figure 3..1. The robust speed controller to be designed is also included in the figure. The essential components in the figure are listed as follows.

- A TMS320C31 digital signal processor (DSP) system board with two on board timers operating at 8.33 MHz (120 ns per tick). The total time required to process the field orientation and the robust speed control subroutine, T_P, is approximately 0.12 ms.
- A three phase voltage source inverter with BJT's having 0 to 100% rise time of 6 μs.
- A safety and debounce circuit. Since the state (ON or OFF) of a BJT cannot be changed instantaneously, a safety circuit is needed to prevent the BJT's within a single branch of the VSI from being ON at the same time. The safety

circuit ensures that $\overline{A}$ is not active until 12 μs after A is deactivated and vice versa. The debounce circuit prevents erratic switching of the inverter caused by transients, at the cost of introducing an undesirable delay T_D of approximately 45 μs.

- An optical shaft encoder with a resolution of 0.1 *degree* (3600 pulses per revolution).
- A counting circuit that processes pulses from the encoder into numbers from 0 to 3599.
- A single cylinder air compressor that provides a periodically varying load to the motor.
- A data buffer circuit for holding the switch vector and rotor position signals.
- A 4 *pole*, 60 Hz, 208 V, 1/3 hp induction motor.

A flow chart of the main program is shown in Figure 3..2. For normal operation, the speed command $\omega^*[k]$ and the rotor position $\varepsilon[k]$, $(k = 0, 1, 2...)$ are sampled at the beginning of each sampling period T_{samp}. The signal $\omega^*[k]$ could be issued by an outer pressure control loop, or simply an asynchronous input from a user interface. The rotor position is used in calculating the rotor speed as $(\varepsilon[k] - \varepsilon[k-1])/T_{samp}$ for robust speed control; and in updating the flux angle for field orientation control according to a discretized version of Equation (2..14). The input and output of the robust speed controller are the speed error signal and the torque command. From

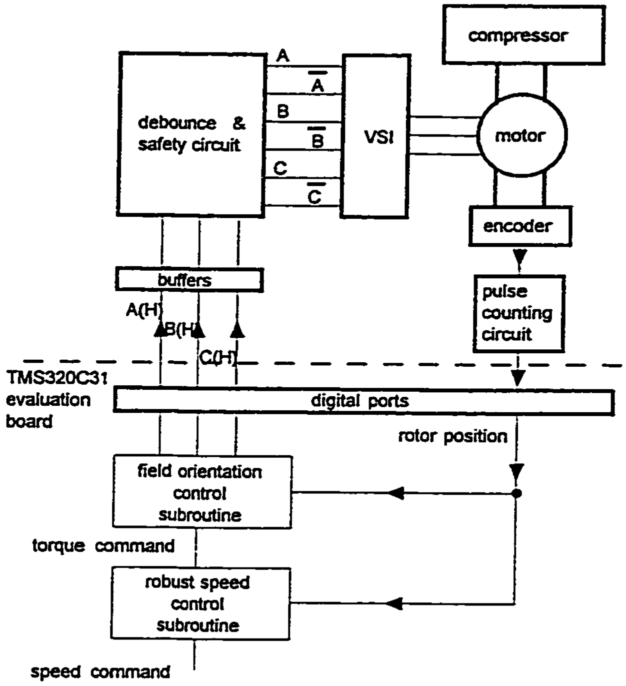

Figure 3..1: Hardware and software arrangements

the torque command and model equations, the field orientation controller computes the required voltage vector to be impressed onto the motor stator. With a voltage source inverter, a time average of the required voltage vector is realized by a computed sequence of switch vectors ($sv1$, ... $sv4$) with appropriate durations ($t1$, ... $t4$). The sum of $t1, ...t4$ must be constrained in the software to be less than T_{samp}.

The timing of the above operations are coordinated by two on board hardware timers, Tmr_0 and Tmr_1. Tmr_0 is used for governing the sampling period T_{samp}; and Tmr_1 is used for setting the durations of various states of the inverter within T_{samp}.

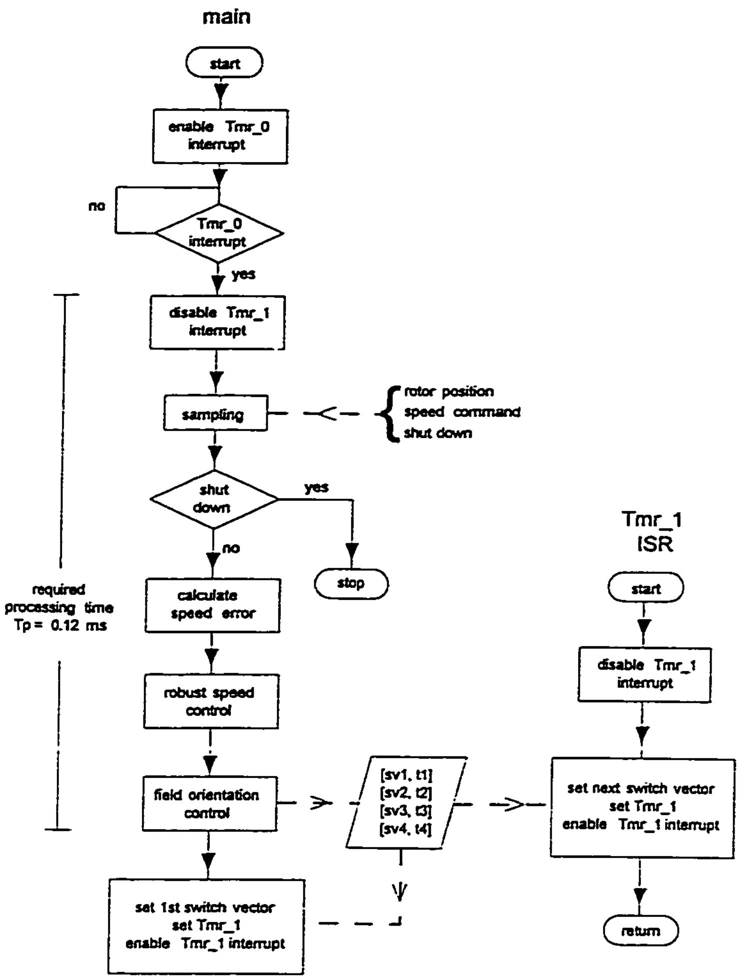

Figure 3..2: Flow chart for control program

3.2 Limits of Signals and Sampling Period

In terms of the flow of important signals, a typical block diagram of a closed loop control system can be constructed as shown in Figure 3..3. Note that u_S (magnitude of $\underline{u}_S$) is limited by hardware while the scalars i^*_{Sd}, i^*_{Sq} and u^*_S are software generated values. With i^*_{Sd} set at a constant value, u^*_S and i^*_S must be properly constrained by software to avoid erratic operations.

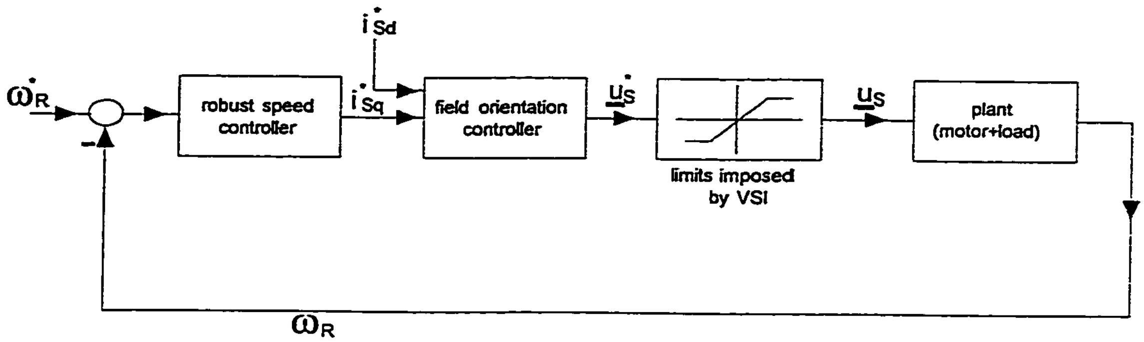

Figure 3..3: Control signal block diagram

For a switch mode realization of u_S^* in a fixed sampling period T_{samp}, a sequence of switch vectors with total duration exceeding T_{samp} will be truncated abruptly with damaging results. The limit of u_S^* in turn affects the choice of the sampling period T_{samp} and the limits of i_{Sq}^*. These constraints are established by the following analysis.

Limit on u_S^* and the Choice of Sampling Interval The realization of a non-zero $\underline{u}_S^*$ requires two non-zero vectors $\underline{u}_x$ and $\underline{u}_y$ to be switched on with durations t_x and t_y respectively ($x, y \in \{1, 2...6\}$). Without loss of generality, assume $x = 1$ and $y = 2$ for the following discussion.

In the ideal case of zero processing time, the magnitude command, $u_{S,ideal}^*$ must be kept small enough at all angle command θ^* so that $(t_1 + t_2) \leq T_{samp}$. For a given u_S within a sector of $0^o < \theta^* < 60^o$, $(t_1 + t_2)$ would become maximum at $\theta^* = 30^o$. In other words, the maximum realizable u_S is at its minimum for $\theta^* = 30^{o1}$. For a

---

[1] For all possible angles between 0^o and 360^o, $Min[Max(u_S^*)]$ occurs at $\theta^* = 30^o + n \times 60^o, n = 0, 1, 2...5$.

given DC link voltage U_{dc} and sampling interval T_{samp},

$$\underset{0<\theta^*<360}{Min}[Max(u_{S,ideal})] = (\sqrt{3})(T_{samp}/2)(U_{dc}/T_{samp}) \approx 0.867U_{dc} \qquad (3..1)$$

In reality, a finite processing time T_P is needed for calculating t_1, t_2 at the beginning of T_{samp}. In addition, a minimum time T_{ON} is required to switch the inverter to output a zero vector near the end of T_{samp}. As a result,

$$\underset{0<\theta^*<360}{Min}[Max(u_S)] = (\sqrt{3})[(T_{samp} - T_P - T_{ON})/2](U_{dc}/T_{samp}) \qquad (3..2)$$

As a consequence of finite T_P and T_{ON}, the theoretical value of $\underset{0<\theta^*<360}{Min}[Max(u_S^*)] = 0.867U_{dc}$ can only be achieved if T_{samp} is infinitely large. Substituting T_P and T_{ON} respectively by $0.125ms$ and $0.006ms$ into Equation (3..2), a plot of $Min[Max(u_S)]/U_{dc}$ versus T_{Samp} is obtained as shown in Figure 3..4.

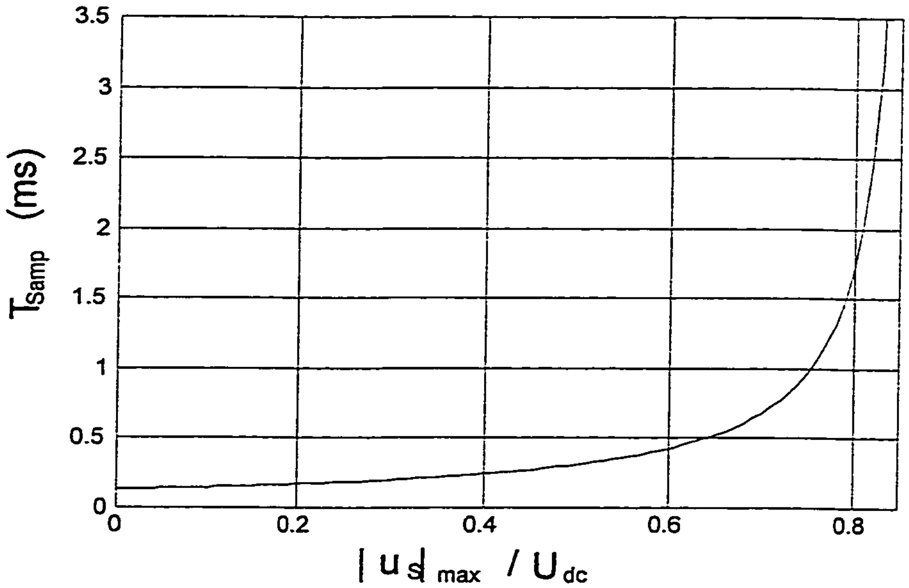

Figure 3..4: Relationship between sampling period and realizable $|u_S|_{max}$

From Figure 3..4, as T_{samp} becomes bigger, $Min[Max(u_S)]$ becomes closer to the ideal value of $0.867U_{dc}$.

The choice of T_{samp} involves trade-offs between the utilization of U_{dc} and the smoothness of motor operating at high speed. Suppose the motor is running steadily at $1800rpm$ (synchronous speed of a 4 pole, $60Hz$ motor), the impressed voltage would ideally be sinusoidal with a period of $16.7ms$ for smoothness in rotation. Therefore, T_{samp} should be many times (say 10) smaller than 16.7 ms. Another consideration is that the smallest electrical time constant[2] associated with the motor is $\tau'_S \triangleq \sigma L_S/R_S$ (0.00557 sec). Therefore T_{samp} should preferably be less than τ'_S to capture the motor dynamics. The choice of T_{samp} equal to $1.5ms$ allows a reasonably balance among the competing constraints. It is about 4 times smaller than the smallest electrical time constant, 10 times smaller than the period of synchronous frequency, and allows a maximum of 79% of U_{dc} (152 V) to be utilized. For a simple linear system design, the output of the speed controller (i^*_{Sq}) should not lead to a u^*_S greater than $0.79U_{dc}$.

Consider the details of a feed forward decoupled indirect field oriented control induction motor shown in Figure 3..5. Since u^*_S is obtained by vector addition in the flux frame, the strategy of clipping of an excessive u^*_S to $0.79U_{dc}$ will lead to a reduction of both torque and flux. Unless carefully backtracked, the estimation of the flux space vector would become erroneous after u^*_S is clipped. The limit of u^*_S should be enforced by constraining i^*_{Sq} properly while maintaining a constant i^*_{Sd}.

---

[2] In indirect field oriented control, the rotor position is required to update the flux space vector position. It is therefore necessary to have a sampling interval compatible with electrical time constants.

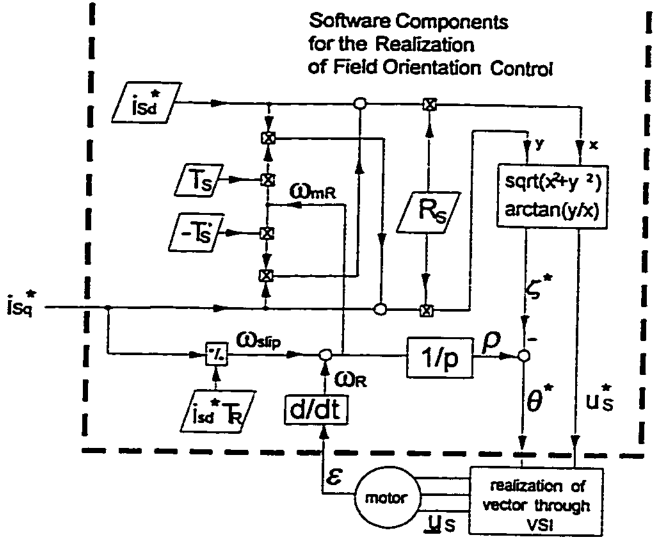

Figure 3..5: Realization of field orientation

Choosing i^*_{Sd} for Constant Flux Operation To efficiently utilize the iron of the motor, i_{Sd} should be maintained at its maximum without excessively saturating the magnetic circuit. This maximum value $max(i_{Sd})$ can be derived from the no load plot of the current phasor $\overline{I}_S$ against an impressed symmetrical three phase voltage $\overline{V}_S$ shown in Figure 3..6. In the figure, $\overline{I}_S$ starts to deviate from its linear trajectory at approximately 0.85 A. Correspondingly from Equation (B.9), $|\underline{i}_S| = 3\sqrt{2}/2 \times 0.85\ A$. Since i_{Sq} is approximately zero at no load, $|\underline{i}_S| \approx i_{Sd}$. To allow fluctuations caused by non-ideal conditions, i^*_{Sd} can be reduced by a factor of say, 0.7. For the motor available for this thesis project, i^*_{Sd} was set at 1.26 A.

Saturation Limit of i^*_{Sq} As discussed previously, i^*_{Sq} must be constrained for limiting u^*_S indirectly for proper switching of the VSI and hence proper operation of the indirect field orientation subroutine. From Figure 3..5, i^*_{Sq} affects the magnitude u^*_S

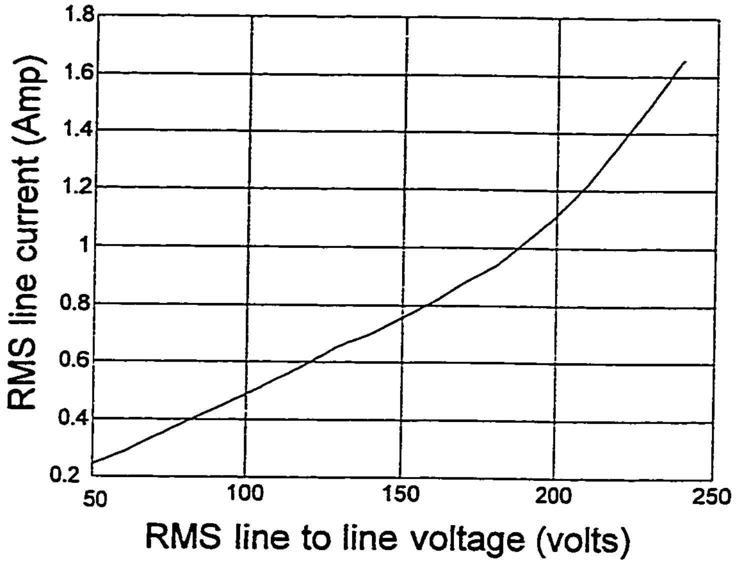

Figure 3..6: Experimental result: $\overline{I}_S$ vs $\overline{V}_S$ under no load

and angle ς^* through the following non-linear equations.

$$(u_S^*) = \sqrt{(R_S i_{Sd}^* - L_S' \omega_m R_S i_{Sq}^*)^2 + (R_S i_{Sq}^* + L_S \omega_m R_S i_{Sd}^*)^2} \tag{3..3}$$

$$\varsigma^* = arctan\left[\frac{(R_S i_{Sq}^* + L_S \omega_m R_S i_{Sd}^*)}{(R_S i_{Sd}^* - L_S' \omega_m R_S i_{Sq}^*)}\right] \tag{3..4}$$

$$\omega_m = i_{Sq}^* / (\tau_R i_{Sd}^*) + \omega_R \tag{3..5}$$

With $i_{Sd}^* = 1.26\ A$ (and motor parameters obtained from experiments), plots of u_S^* against i_{Sq}^* at different values of the rotor speed ω_R are shown in Figure 3..7. It can be seen that for a hardware limit of $u_S^* = 151.7\ V$, the limit of $Max(i_{Sq}^*)$ varies linearly with the rotor speed. For example, at 1000 rpm, i_{Sq}^* should not exceed 9.5 A otherwise the limit of u_S^* would be violated and results in erroneous switching sequence. At

1800 *rpm*, i^*_{Sq} should be limited at 6.8 A. From Equations (3..3) and (3..5), it is clear that the speed variant nature of the i^*_{Sq} saturation limit is caused by the decoupling terms $-L'_S\omega_{mR}R_S i^*_{Sq}$ and $L_S\omega_{mR}R_S i^*_{Sd}$. Since $L_S > L'_S$, the expression on the right hand side of Equation (3..3) increases with increased ω_R. When the expression is constrained by the hardware limit, i^*_{Sq} must be decreased with increased ω_R.

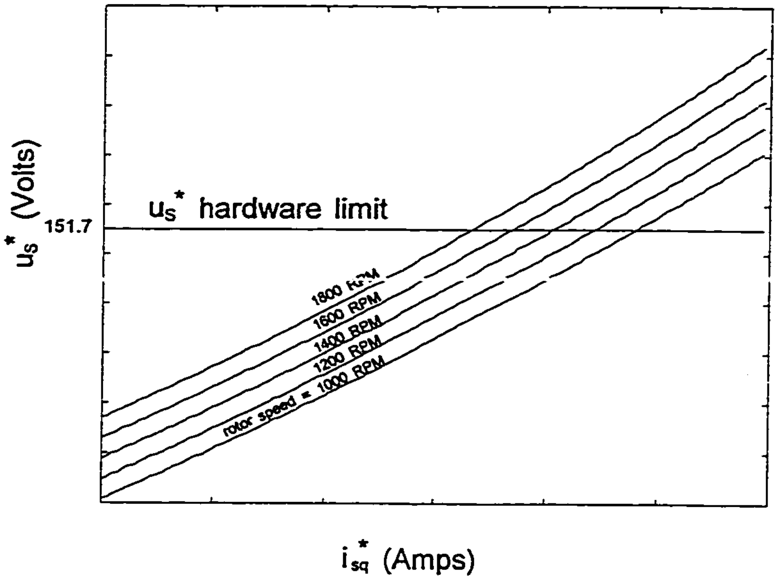

Figure 3..7: Limits of $Max(i^*_{sq})$ at different rotor speeds

From the allowable $Max(i^*_{Sq})$, the maximum electromagnetic torque available at various rotor speeds can be calculated from Equation (2..11). The linear maximum realizable torque versus ω_R curve plotted in Figure 3..8, together with the curve for the rated power of the motor, define the steady state, safe operating region of the VSI driven FOC-IM (shaded area).

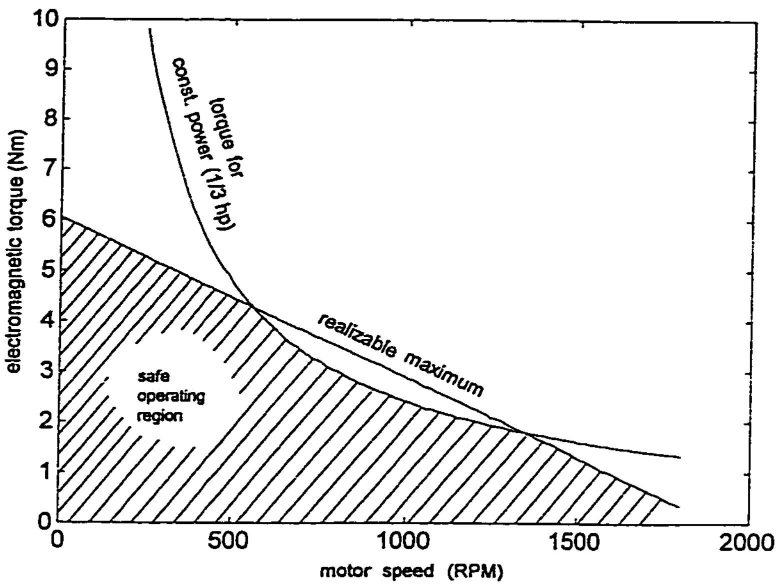

Figure 3..8: Maximum realizable torque versus rotor speed

3.3 Input-Output Characterization of the FOC-IM

For indirect field oriented control, proper field orientation can only be verified indirectly. A simple verification can be based on the fact that if $i_m = i_{Sd}^* = I_{Sd}$ and field orientation is properly performed, then from Equations (2..11) and (2..22), the VSI driven indirect FOC-IM would have the following linear input-output characteristics

$$tf : i_{Sq}^* \mapsto T_e = \frac{K_t}{(\tau'_S p + 1)} \qquad K_t = \left(\frac{P}{2}\right)\left(\frac{2}{3}\right)\frac{L_o}{(1+\sigma_R)} I_{Sd}^* \tag{3..6}$$

And for a motor with a cylindrical rotor, the torque to speed transfer function can be approximated by

$$tf : T_e \mapsto \omega_R = \frac{1}{(J_{motor}p + B_{motor})} rad/Nm.s. \tag{3..7}$$

where J_{motor} and B_{motor} are constants. It follows that if there are no torque disturbances,

$$tf : i^*_{sq} \mapsto \omega_R \triangleq G_{FOC} = \frac{K_t}{(\tau'_S p + 1)(J_{motor}p + B_{motor})} rad/A.s. \tag{3..8}$$

The approach adopted in this project for the verification of proper field orientation is as follows.

- Establish the parameters of the model stated in Equation (3..8).
- Verify model predictions by experiments performed on hardware.

Establishing the no load input-output model In Equation (3..8), K_t and τ'_S are well defined by resistances, inductances and leakages obtained from standard tests. Assume the no load model is a 'good model', then for $i^*_{Sq} = I^*_{Sq} \times 1(t)$,

$$B_{motor} = \frac{K_t I^*_{Sq}}{\omega_R]_{t\to\infty}}$$

Experimental observations of B_{motor} versus ω_R are shown in Figure 3..9. Assume during operation, speed variations occur in the range of 25 to $180 rad/s$, it is practical to cover this operating range without being over conservative by setting $B_{motor} = 2.5 \times 10^{-4} Nmsec \pm 20\%$.

To find J_{motor}, the transient response of ω_R to $I^*_{sq} \times 1(t)$ can be inspected.

$$\omega_R = \frac{T_e}{B_{motor}} \left[1 + \frac{\tau'_S e^{-t/\tau'_S}}{(J_{motor}/B_{motor}) - \tau'_S} - \frac{(J_{motor}/B_{motor}) e^{-t/(J_{motor}/B_{motor})}}{(J_{motor}/B_{motor}) - \tau'_S} \right]$$

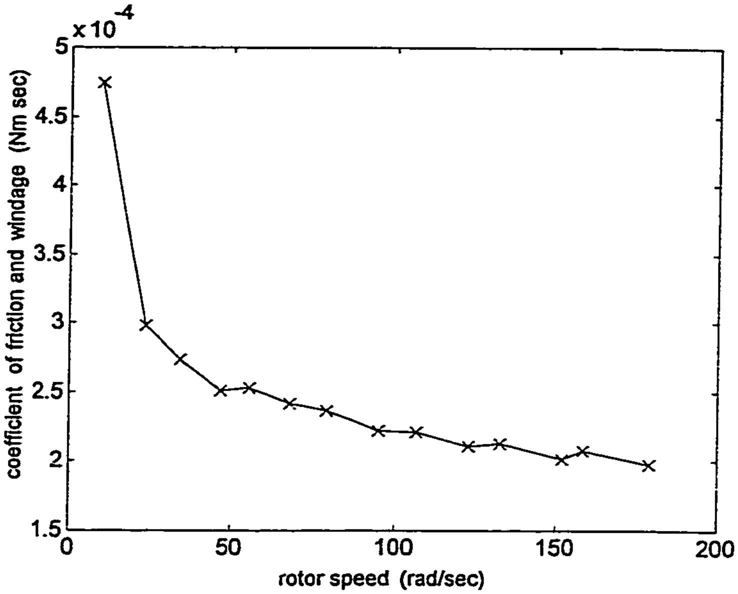

Figure 3..9: Coefficients of friction and windage for the motor calculated from experimental data

where $T_e = K_t I_{sq}^*$.

The effect of τ'_S on ω_R becomes insignificant when $t > 5\tau'_S$ in the above equation. Suppose $J_{motor}/B_{motor} >> \tau'_S$, then for $5\tau'_S < t << J_{motor}/B_{motor}$, $e^{-t/(J_{motor}/B_{motor})} \cong 1$ and

$$d\omega_R/dt \cong T_e/J_{motor} \Rightarrow J_{motor} \cong \frac{T_e}{\Delta\omega_R/\Delta t}$$

This can be seen in Figure 3..10 for an $i_{Sq}^*(t) = 0.5 \times 1(t)\ A$, J_{motor} is approximately $0.001804 Nm.s^2$.

In summary, Equation (3..8), has the following estimated parametric values.

- $K_t = 0.47\ Nm/A$, calculated from values obtained from standard no load and locked rotor tests.

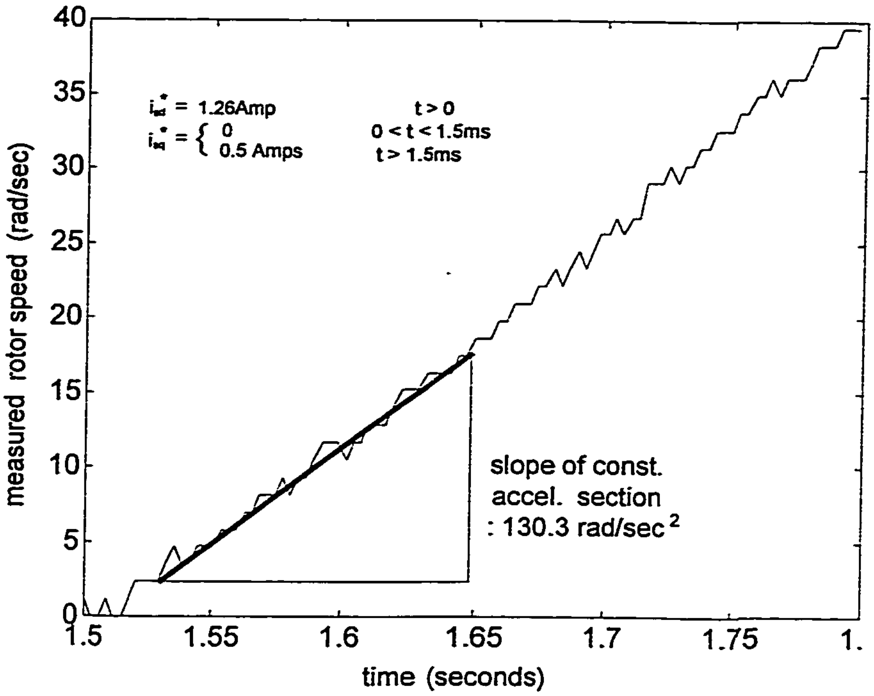

Figure 3..10: Estimation of J_{motor} from step response data

- $\tau'_S = 0.0049\ s$, calculated from values obtained from no load and locked rotor tests.

- $B_{motor} = 0.00025\ Nm.s$, obtained from a single experiment.

- $J_{motor} = 0.001804\ Nm.s^2$, obtained from a single experiment.

Model Verification The linear nature predicted by Equation (3..8) is verified qualitatively by observing the shape of the outputs upon sinusoidal inputs. In Figure 3..11, there are three sets of normalized input and output trajectories. The inputs are discrete sinusoids

$$i_{sq}^* = I_{sq}^* sin(2\pi f k T), \quad k = 0, 1, 2...$$

where $f = 1$, 2 and $4Hz$, $T = 0.15ms$ and $I^*_{sq} = 0.5A$. It can be seen that the trajectories of ω_R are fairly close to being sinusoidal.

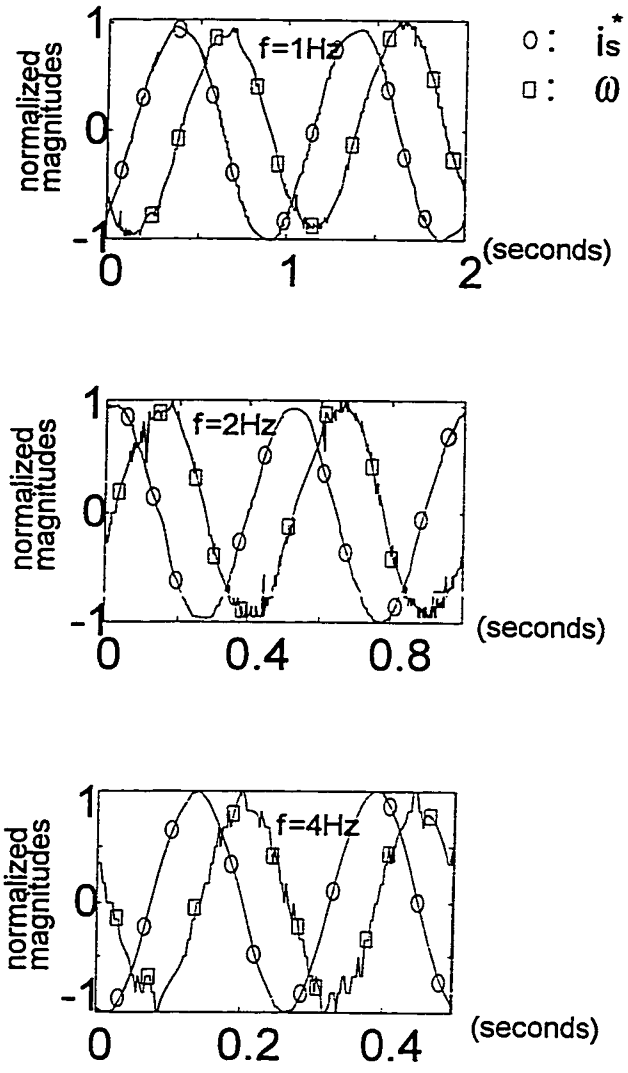

Figure 3..11: Normalized frequency response data for verification of linear behavior

Note that since there are no load attached to the motor, only signals with small amplitude and low frequencies can be used in the tests to avoid overspeeding. A leap of faith is required for treating the true plant as linear when i^*_{Sq} is significantly larger than $0.5A$. To verify linearity of the model if $i^*_{sq} > 0.5A$, step responses for short intervals can be used. In Figure 3..12, step responses of ω_R with i^*_{sq} varying from $0.1A$ to $1.5A$ (again, limited to avoid overspeeding) are plotted. It can be seen that for each increment of $0.1A$ in i^*_{sq}, ω_R at any given time shown in the figure is increased by approximately the same amount. Moreover, the electromagnetic torque generated reached its command value almost 'instantaneously' since no significant change of slope can be observed in any of the speed trajectories.

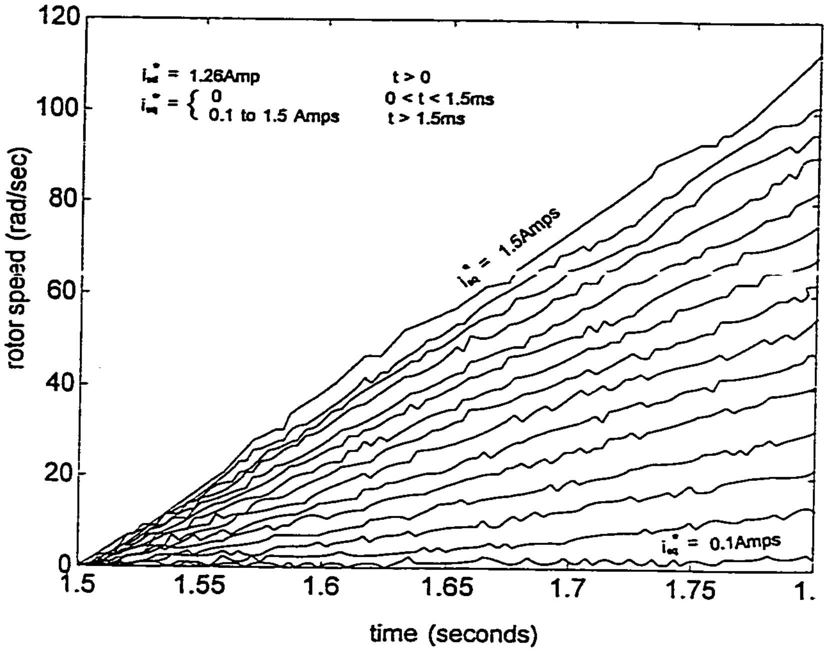

Figure 3..12: Verification of linear behaviour from step response data

From the sinusoidal and the step responses, it can be concluded that the input-output map of the FOC-IM is reasonably linear as predicted by Equation (3..8).

The model can be further verified by comparing the predicted step response of ω_R to hardware results. The comparison is shown in Figure 3..13. It can be seen that the predictions and experimental results agree with each other for i^*_{sq} larger than 0.5A. The deviations of experimental results at low magnitudes of i^*_{Sq} from predictions are expected because the B_{motor} parameter in the model is chosen as a constant suitable for high speed operations.

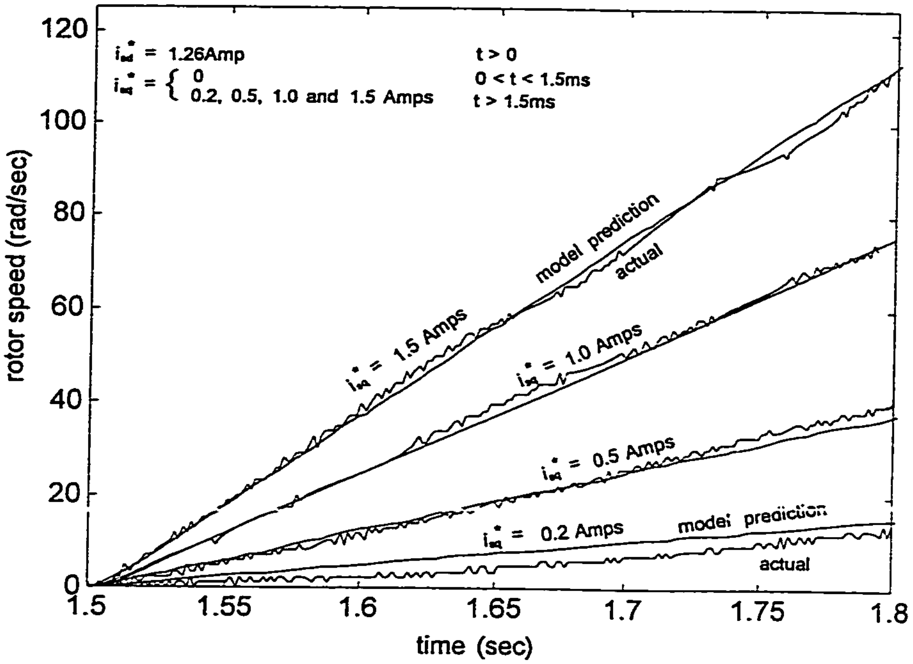

Figure 3..13: Comparison of measured speeds to model predictions

From the above analysis of experimental results, it can be concluded that the motor behaves as predicted by field orientation and thus the model established in Equation (3..8) is suitable for control system design.

3.4 Operations under Detuned Conditions

The stator resistance R_S and rotor resistance R_R of a motor can vary by a significant amount during operation. Denoting the estimations of these resistances by $\widehat{R}_S$ and $\widehat{R}_R$, this section presents the investigations in the behavior of a VSI driven

FOC-IM when $[\widehat{R}_S, \widehat{R}_R]$ are different from $[R_S, R_R]$.

The purpose of the investigation is to determine if detuned operations can still be represented by the LTI model of Equation (3..8) and to examine how the K_t parameter may change in Equation (3..8) under detuned conditions.

Note that $K_t = \left(\frac{P}{2}\right)\left(\frac{2}{3}\right)\frac{L_o}{(1+\sigma_R)}i^*_{Sd}$ (from Equation (3..6)) is valid only when field orientation is properly performed. The tolerance of K_t under detuned conditions should not be found directly from the tolerances of L_o and σ_R.

In actual operations, $[R_R, R_S]$ changes according to temperature while $[\hat{R}_S, \hat{R}_R]$ remains constant in software. However, it is difficult to conduct the investigation by changing the rotor resistance of a cage motor. An alternative is to run the motor under no load until it is warm and assume $[R_R, R_S]$ remains constant thereafter. Subsequently, $[\hat{R}_R, \hat{R}_S]$ are then changed to different values in the field orientation subroutine. Such a strategy is employed in an investigation using simulations. The results of which are verified qualitatively by experiments[3] on the actual plant.

Effects of error in rotor resistance Using the simulation program listed and explained in Appendix C, the simulated results for $\hat{R}_S = R_S$ and $\hat{R}_R \neq R_R$ were obtained as shown in Figure 3..14.

A remarkable feature in Figure 3..14 is that the average T_e is not maximized when $\hat{R}_R = R_R$. In fact if $\hat{R}_R > R_R$, T_e would fluctuates but assumes values larger than that generated by correct field orientation. This behavior provides a guideline

---

[3] For the lack of a suitable torque meter and associated equipment, the predition of torque trajectories from simulations can only be inferred from the observations of speed in experiments.

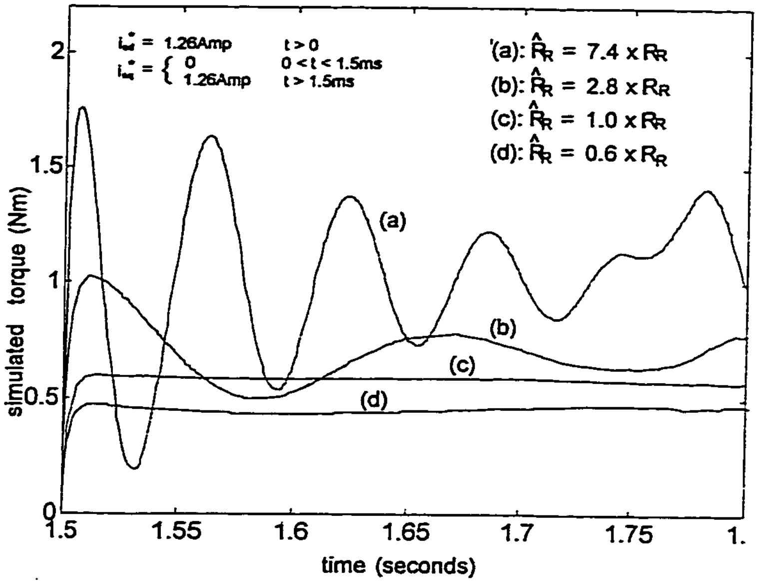

Figure 3..14: Simulation of T_e for various $\hat{R}_R$ values of a VSI driven FOC-IM

for tuning $\hat{R}_R$ off line.

The above qualitative predictions were verified by speed trajectories observed in experiments. Shown in Figure 3..15 are four sets of speed trajectories corresponding to the simulations discussed above. Curve (c) is the best field orientating performance achievable as far as matching $[\hat{R}_R, \hat{R}_S]$ to $[R_R, R_S]$ is concerned.

Regarding the speed trajectory (a) for which $\hat{R}_R$ is deliberately set many times larger than R_R, the unsteady acceleration of the rotor clearly shows that T_e is fluctuating as predicted by the simulations. Furthermore, since the slope of curve (a) is larger than that of curve (c), the T_e that generates curve (a) is larger. For curve (d) in Figure 3..15, $\hat{R}_R$ was set at a value less than R_R. T_e, although less than that generated under matched conditions, has a steady value as shown by the constant acceleration of the rotor.

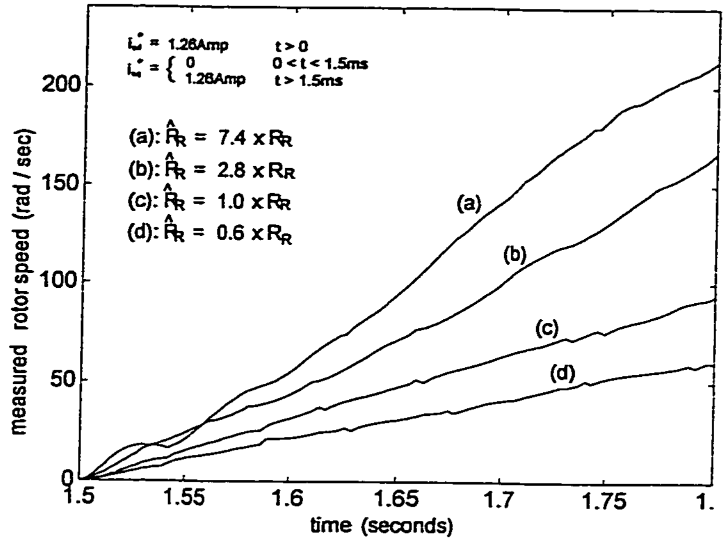

Figure 3..15: Rotor speeds measured under detuned $\hat{R}_R$ conditions

Strategy in setting $\widehat{R}_R$ and $\widehat{R}_S$ A second remarkable feature in Figure 3..15 is that when $\hat{R}_R < R_R$, T_e becomes smaller but remains relatively constant. This implies that if $\hat{R}_R$ is set equal to the value measured at the lowest operating temperature, the feedforward decoupled indirect FOC-IM can suitably be represented by Equation (3..8) at all other operating temperatures, perhaps with a degradation in the steady state gain K_t. Expecting R_R and R_S will be perturbed in the same direction under operating conditions, simulations are performed for cases where $\hat{R}_R < R_R$ and $\hat{R}_S < R_S$. The simulated values of T_e and the rotor speed from corresponding hardware experiments are shown in Figure 3..16.

The results indicate that **the electromagnetic torque can be still considered as instantaneous and steady whenever $\hat{R}_R < R_R$ and $\hat{R}_S < R_S$.** Furthermore, the steady state gain K_t becomes smaller as R_R and R_S increase with the motor temperature. Clearly, the tolerance of K_t depends on the cooling arrangements for the motor.

Extended Operations under Constant Torque Command The simulations and experiments discussed so far are limited to a very short duration of 0.3 seconds. This is because under a constant torque command, the motor under no load would accelerate beyond safe speed limits in extended operations. With the confidence of the simulator established by the matching results of hardware experiments, it becomes feasible to investigate by simulation the torque transients of the indirect VSI driven FOC-IM for step inputs of torque commands. The simulated results for different settings of $[\hat{R}_R, \hat{R}_S]$ are shown in Figure 3..17.

Over an extended interval, simulations show cyclic variations of the generated torque in response to a step command. The unsteadiness is thought to be caused by the inaccuracies in the flux estimation induced by the sampling period, as well as the inaccuracies of the inverter in the realization of an angle command shown in Appendix E.

3.5 Discussion

Verification of Field Orientation The ultimate goal of field orientation is to achieve an instantaneous, zero dynamic torque response to a command. All variables in equations are means to an end. In fact, some of the variables cannot even be measured directly or accurately with conventional equipment. Proper field orientation should therefore be verified by its intended effects, i.e. the torque generated by the motor in response to a command. Given an accurate torque meter is available, proper field orientation can be verified by the 'instantaneous step change' of torque in response to a step command.

Direct observations on the time trajectory of T_e require expensive equipment, especially when the motor is rotating. Because of limitations in budget, observations of the motor speed are used for verification of field orientation. Interesting indirect verification procedures from the trajectories of current amplitude, phase and frequency can be found in [H2].

Saturation Limits If saturation limits of actuators are neglected, an otherwise normal system may oscillate to extremes when the controller output is larger than the limits. This is known in the industry as the integrator windup problem. For a constant limit, a simple practice is to ensure the (speed) controller generates an output (in this case i^*_{Sq}) that is always less than the limit. Normally the design is performed by scaling the signals with their largest expected perturbations. For better performance, a non-linear technique known as saturation feedback in Appendix F could be employed[M2].

The speed variant limit on i^*_{Sq} shown in Figure 3..8 presents an unusual problem for the design of a closed loop system. In short, the design procedure of scaling the controller output signal by the saturation limit becomes ambiguous. Since the speed variant limit on i^*_{Sq} is imposed by the constant limit on u^*_S, a brute-force method is to provide a command filter so that for the largest input step command, the controller output will never lead to an excessive u^*_S.

3.6 Summary

In section 3.1, an implementation for a VSI driven FOC is described. In section 3.2, signal limits on u_S^*, i_{Sd}^*, i_{Sq}^* and choice of the sampling period T_{samp} for this implementation are investigated and established. The unusual speed variant limit of i_{Sd}^* are discovered and the solution by command filtering is proposed. In section 3.3, the input-output model of the implementation under nominal conditions is established and verified. Operations under detuned conditions are presented in section 3.4. The results show that if the parameters $\widehat{R}_R$ and $\widehat{R}_S$ are properly set, the input-output model established in section 3.3 may still be used for linear control system design.

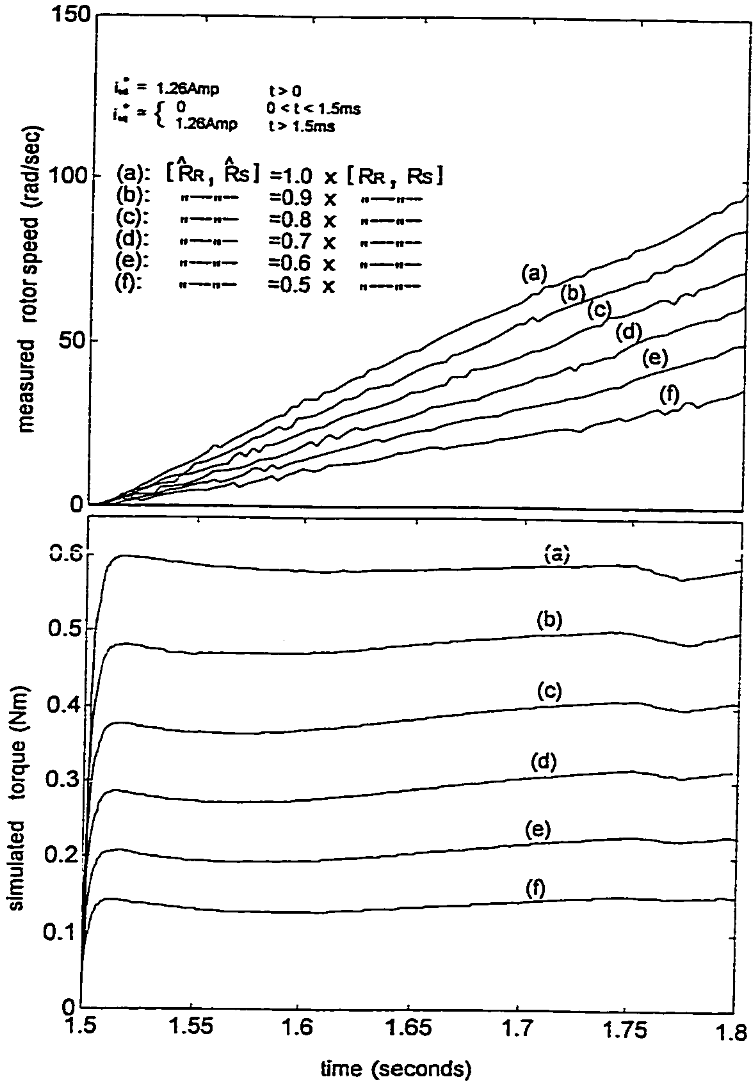

Figure 3..16: Measured speeds and simulated torque generated (R_S and R_R both perturbed)

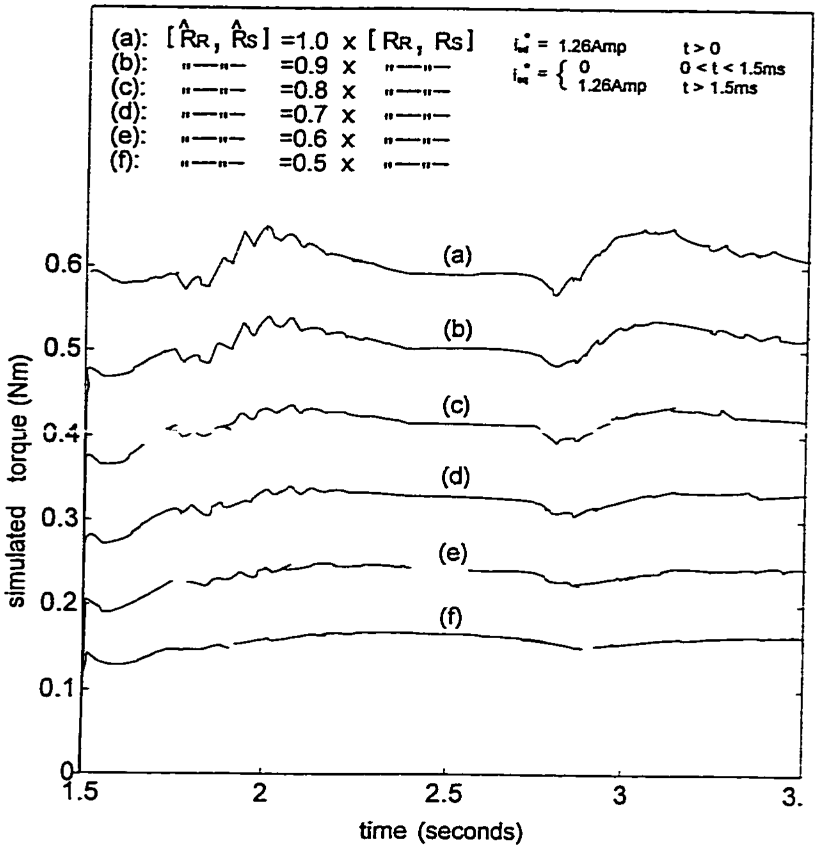

Figure 3..17: Simulated T_e generated in extended intervals, (R_S and R_R both perturbed)

CHAPTER 4.

INTRODUCTION TO ROBUST CONTROL

Depending on the objectives, control system analysis or design starts with modelling the *relevant* behaviors, G_{true}, of a physical plant by a *tractable* nominal model G_{nom}. Because of limitations in mathematics, G_{true} is invariably much more complicated than G_{nom}. The fact that $G_{nom} \neq G_{true}$ can be viewed as G_{nom} being uncertain. The uncertainties, Δ_u, may be caused by parameter changes, neglected dynamics, or other effects in the modelling process. In classical control design, gain and phase margins are used primarily to quantify the robustness of the system against Δ_u. However, while the tolerable Δ_u are implied by the gain and phase margins, there are no attempts to quantify Δ_u explicitly in the classical design process. The amount of gain and phase margins incorporated in designs is based on experience, rules of thumb and sometimes trial and error.

The robust control problem can be loosely stated as follows: **Given the performance specifications for a system with sensors and actuators, design a controller to meet the specifications for a well defined set of models.** There are many approaches to this problem. Some common labels are $\mathcal{H}_\infty$, μ, Kharitonov and QFT. This chapter presents some of the basics in $\mathcal{H}_\infty$ control that will be used in the plant modelling and controller design processes. Most of the material introduced in this chapter are interpretations from the books of Doyle[D1] and Zhou[Z1].

4.1 Modelling with Multiplicative Unstructured Uncertainties

Uncertainties always exist in a nominal model G_{nom}. By incorporating the uncertainties associated with G_{nom} to form a set of plants $\tilde{G}$, it is hoped by a designer that G_{true} is contained within the set; and by designing a feedback system for $\tilde{G}$ rather than just G_{nom}, the closed loop system resulted would operate according to specifications under all foreseeable model perturbations. In $\mathcal{H}_\infty$ control, it is common to use the so called multiplicative unstructured uncertainty for modelling $\tilde{G}$:

$$\tilde{G} = (1 + \Delta W_2)G_{nom} \tag{4..1}$$

where W_2 is a fixed stable transfer function whose magnitude is an upper bound of all possible deviations from the magnitude of G_{nom}; and Δ is a variable stable transfer function whose maximum magnitude is less than or equal to 1.

In Figure 4..1, the magnitude response of some probable nominal plant G_{true}, G_{nom} and $\tilde{G}$ are shown. It is assumed that the relevant behaviors (G_{true}) of the physical plant can be considered as a linear system whose trajectory can be anywhere bounded by the shaded region. Note that the nominal model G_{nom} need not be a member of G_{true}. The choice of G_{nom} depends mostly on insights on the system such as the knowledge of the most frequently encountered operating conditions.

4.2 Frequency Weighted Design Objectives

Nominal Performance Objective Consider the closed loop control system shown in Figure 4..2.

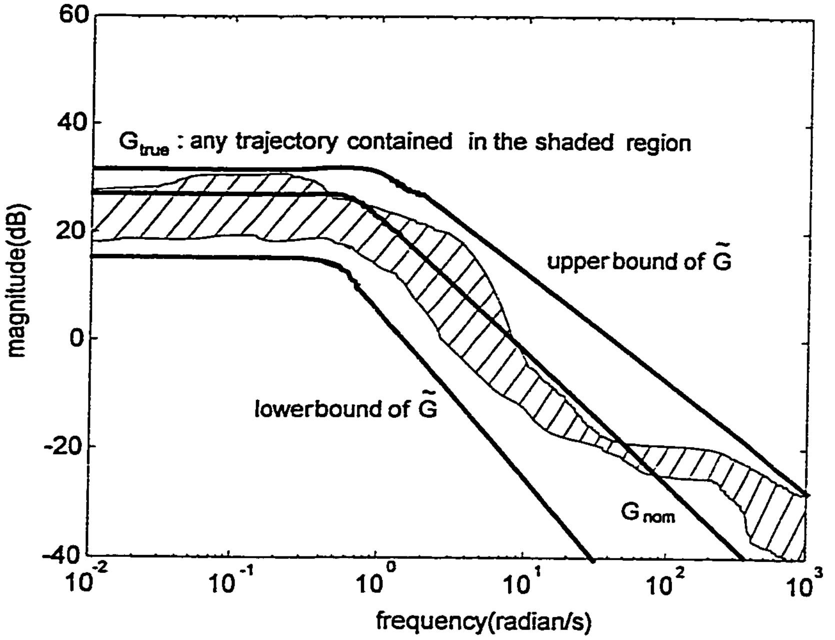

Figure 4..1: Relationships between G_{true}, G_{nom} and $\tilde{G}$

The figure consists of a nominal plant G_{nom} and a compensator K. The signals r, n and d, exogenous to the plant, are the command, noise and equivalent output disturbance respectively; and u is the control signal. Let the open loop transfer function be $L \triangleq KG_{nom}$. Then the Bode sensitivity function S and the complementary sensitivity function T are defined as $S \triangleq 1/(1+L)$ and $T \triangleq L/(1+L)$. Naturally, the identity

$$S + T = 1 \tag{4..2}$$

imposes a constraint on the sizes of S and T. The system shown, if stable, has the following major properties:

$$y = T(r-n) + Sd \tag{4..3}$$

$$e = r - y - n = S(r - n - d) \tag{4..4}$$

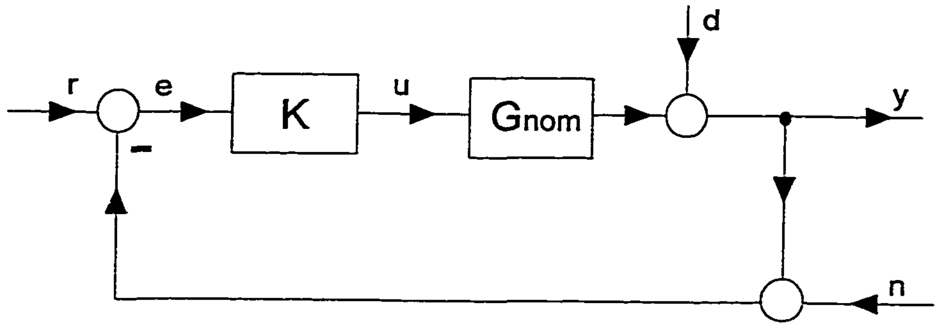

Figure 4..2: A typical unity feedback control system

$$\frac{\Delta T}{T} = S\frac{\Delta L}{L} \tag{4..5}$$

where $\Delta T/T$ denotes the relative change in the closed loop transfer function T and $\Delta L/L$ the relative change in the open loop transfer function L, caused by change in the plant.

From Equations (4..3),(4..4)and (4..5), S is desired to be small for disturbance rejection, command tracking, and small sensitivity. However, from Equation (4..3), T is also desired to be small for measurement noise rejection at the output. With the constraining identity (4..2), S and T cannot be both small at any frequency.

Fortunately, n is usually prominent at high frequencies while r and d are more significant at low frequencies. If so, disturbance rejection, command tracking and sensitivity reduction can all be achieved by suppressing S at low frequencies. These objectives can be expressed as an inequality constraint on the infinity norm $\| W_1 S \|_\infty < \gamma$ [1], where W_1 has a magnitude response resembling that of a low pass filter. When

---

[1] The infinity norm $\|G\|_\infty$ of a single-input, single-output transfer function G is equal to the supremum of the magnitude response of G.

scaled by γ, a standardized form of nominal performance specification is obtained as

$$\| \, W_1 S \, \|_\infty < 1 \tag{4..6}$$

Robust performance criteria To achieve robust performance, a closed loop system must achieve the inequality (4..6) for $\tilde{G}$ instead of just for G_{nom}. The following necessary and sufficient condition proved in [D1] is useful as a test for robust performance.

$$\| \, |W_1 S| + |W_2 T| \, \|_\infty < 1 \tag{4..7}$$

The design task is therefore to find a controller so that the closed loop system will satisfy inequality (4..7). The transfer functions G_{nom}, W_1 and W_2 are the design inputs and the compensator K is the design output. Such a K may not exist for any triplet (G_{nom}, W_1, W_2).

4.3 Loop Shaping

Unfortunately, there are no known theories to predict the existence of, nor methods for synthesizing the controller that satisfies inequality (4..7) without conservativeness. For minimum phase plants with non-stringent performance requirements, a satisfactory controller may be found by a loop shaping technique presented in [D1]. In short, a suitable magnitude response of the open loop transfer function L is constructed directly; or indirectly by constructing K. When the $|W_1|$ is small at high frequencies $|W_2|$ is small at low frequencies, the following guidelines for loop shaping applies.

- guideline 1. $|L| > |W_1|$ at low frequencies.

- guideline 2. $|L| < 1/|W_2|$ at high frequencies.

- guideline 3. $|L|$ **has a 'smooth' transition at the vicinity of cross over.**

- guideline 4. L has a relative degree larger or equal to the relative degree of nominal G_{nom}.

The closed loop system thus obtained is then checked for stability by either Bode plot or Nyquist stability criterion; and inequality (4..7) verified by substituting S with $1/(1+L)$ and T with $L/(1+L)$. Finally, if L is constructed directly, K is recovered by the equation $K = L/G_{nom}$. When a satisfactory controller cannot be found regardless of its existence, the requirements of W_1 must be relaxed.

4.4 Discussion

Cautions in gain and phase margins It is well known that ample gain and phase margins need not be indications of ample stability margin. In practice, the 'excess phase' at frequencies below the gain cross over and the 'excess gain' at frequencies between gain and phase cross over should be inspected for robustness in stability.

Cautions in $\mathcal{H}_\infty$ optimal design Note that the requirement of L having a smooth transition at cross over is related to the classical phase margin of the system. The phase margin in turn, is viewed conventionally as an important parameter that relates to the time domain performance in step tracking. Systems with sufficient phase margin will have less overshoot and fast settling time in response to a step command.

In $\mathcal{H}_\infty$ optimization, if W_1 and W_2 are represented in closed forms, algorithmic procedures such as the "Two Riccati Equation Method" by Doyle and Glover can be used for synthesizing a controller that optimizes the nearby specification:

$$\| \, |W_1 S|^2 + |W_2 T|^2 \, \|_\infty < 1 \tag{4..8}$$

However, it is difficult, if not impossible, to incorporate the condition of "smooth" cross over of L into a closed form frequency domain objective. In many cases, a good controller cannot be obtained from the optimization of (4..8).

For some systems, (especially a MIMO system) the problem of obtaining good performance from algorithmic procedures operating on weighted frequency objectives become more serious. There is a tendency to treat W_1 and W_2 as design parameters without any physical bases (pp.87, [Z1]), and select the weights in an ad hoc manner through iterations and fine tuning (pp.89, [Z1]). In order to avoid such processes for a relatively simple SISO design, the author chose to design the system according to the four guidelines of loop shaping listed in the previous section.

4.5 Summary

The principles and techniques of using multiplicative unstructured uncertainties for modelling a plant are introduced. The meaning of robust performance, and guidelines to use loop shaping for the design of a robust control system are presented.

CHAPTER 5.

DESIGN AND IMPLEMENTATION OF ROBUST SPEED CONTROLLER

This chapter deals with the details in the modelling of the combined VSI driven FOC-IM and reciprocating compressor as a plant, as well as the design and implementation of the robust speed controller.

5.1 Literature Review

With both the field oriented control and the robust control theories being current results of different research communities, there are only a few recent publications in the design of a robust speed controller for an FOC-IM ([L3], [L5], [L4]and [T2]). Both [L3] and [L5] did not address the model uncertainties explicitly; [L4] obtained an $\mathcal{H}_\infty$ optimal controller using functions provided in the robust control toolbox of MatLab. However, no justifications are given as to the frequency weights selected. [T2] achieves robust performance by augmenting an $\mathcal{H}_2$ optimal internal model controlled system with a robust compensator. This thesis project attempts to obtain a robust design directly by loop shaping.

5.2 Proposed Nominal Plant Model

It is well known in dynamics that for a torque T_e driving a load with inertia J_L and coefficient of friction B_L, the following torque-speed relationship applies:

$$T_e = T_d + J_L \frac{d\omega_R}{dt} + B_L \omega_R \qquad (5..1)$$

where T_d is the load torque and ω_R the angular speed.

Without further information, T_d can be considered as an external disturbance to be rejected by the system

$$T_e = J_L \frac{d\omega_R}{dt} + B_L \omega_R. \tag{5..2}$$

If J_L and B_L can be considered as constants, the mapping $T_e \mapsto \omega_R$ is LTI.

$$G_L \triangleq tf : T_e \mapsto \omega_R = \frac{1}{J_L p + B_L} \tag{5..3}$$

Assuming negligible loading effect of the compressor on the performance of the FOC-IM, G_L can be cascaded with G_{FOC} to form

$$\begin{aligned} G_{ideal} &\triangleq tf : i^*_{sq} \mapsto \omega_R \\ &= G_L G_{FOC} \\ &= \frac{K_t}{(\tau'_S p + 1)(J_{motor} p + B_{motor})(J_L p + B_L)} \\ &\cong \frac{K_t}{(J_L p + B_L)} \quad Since \frac{J_L}{B_L} >> \frac{J_{motor}}{B_{motor}} >> \tau'_S \end{aligned} \tag{5..4}$$

Conformance to Model by Feedback Linearization The approximation in Equation (5..4) is adopted to avoid complications in model verification due to the nature of J_L and B_L(explained next). By dropping the term $1/(\tau'_S p+1)(J_{motor} p + B_{motor})$, the size of W_2 (model uncertainty) is expected to become larger as a trade off for the ease of obtaining a nominal plant model.

The proposed LTI model is appropriate for plants with constant J_L and B_L. For a reciprocating compressor equipped with a massive flywheel, J_L may be approximated by a constant. However, due to frictions between journals and shell type bearings, B_L varies with speed significantly.

To investigate, the sequence $i^*_{Sq} = \{0.76, 0.78, ...1.28\}$ and its reverse are employed to obtain the quasi-static relations between ω_R and i^*_{Sq}. The results are shown in Figure 5..1. As the speed is lowered, the thickness of the oil film separating the journal and bearings would become thinner. Eventually the journals and bearings within the compressor would come into contact with each other. This phenomena would lead to a sudden, significant increase of resistance to motion and the speed would drop to zero. From experiments, it is found that rotating motions cannot be maintained at constant speeds below 17 rad/s.

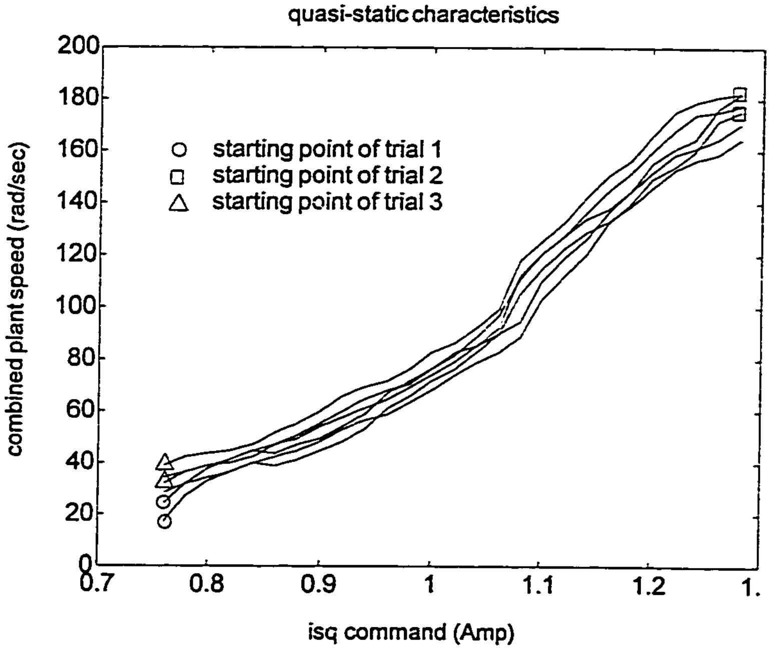

Figure 5..1: Static relationsips between i^*_{Sq} and rotor speed obtained from experiments

From Equation (5..4), the values of $B_L = Kt \times i^*_{Sq}/\omega_R]_{t\rightarrow\infty}$ at various speeds are calculated. It is found that the spread of B_L is more than an order of magnitude. Assuming B_L is related to ω_R, it is possible and desirable to modify the physical plant by feedback linearization.

Let $B_{Lnom} = 0.0035$ corresponds to $\omega_0 = 175\ rad/s$, then for $\omega_R \leq \omega_0$, $B_L = B_{Lnom} + \Delta B$, where ΔB is a function of $(\omega_0 - \omega_R)$. With a compensating current i_{Comp}, the equation that describes the motion of the plant is

$$J_{Lnom}\,\dot{\omega}_R + [B_{Lnom} + \Delta B_L]\omega_R = K_t(i^*_{Sq} + i_{Comp})$$

By using the feedback compensation $i_{Comp} = \Delta B_L \times \omega_R / K_t$, the map $i^*_{Sq} \mapsto \omega_R$ would conform to Equation (5..4). Without further information, ΔB_L is assumed to be a polynomial, the values of $(B_L - B_{Lnom})$ are plotted against $(\omega_0 - \omega_R)$ and a second degree polynomial[1] is fitted as shown in Figure 5..2.

$$\begin{aligned}
\Delta B_L &= a_2(\Delta\omega)^2 + a_1(\Delta\omega) + a_0 \\
\Delta\omega &= \omega_0 - \omega_R, \quad \omega_0 = 175 \quad rad/s. \\
[a2, a1, a_0] &= [2.8147e^{-7}, -4.0393e^{-6}, -1.8128e^{-4}] \qquad (5..5)
\end{aligned}$$

Schematically, the linearization would be implemented as shown in Figure 5..3.

As a result, B_L for the feedback linearized plant may now be approximated by the constant B_{Lnom}. The spread of B_L before and after linearization are shown in Figure 5..4.

---

[1] A better fit had been obtained with a 5^{th} degree polynomial. The results were however erratic. It is suspected that problems were caused by truncation errors in calculating products of very large numbers, $(\Delta\omega)^5$, and small coefficients. It is also likely that B_L is a function related to higher derivatives of $(\Delta\omega)$ and other unknown phenomena. The use of a 2^{nd} degree polynomial for feedback compensation can only be justified as a means to an end.

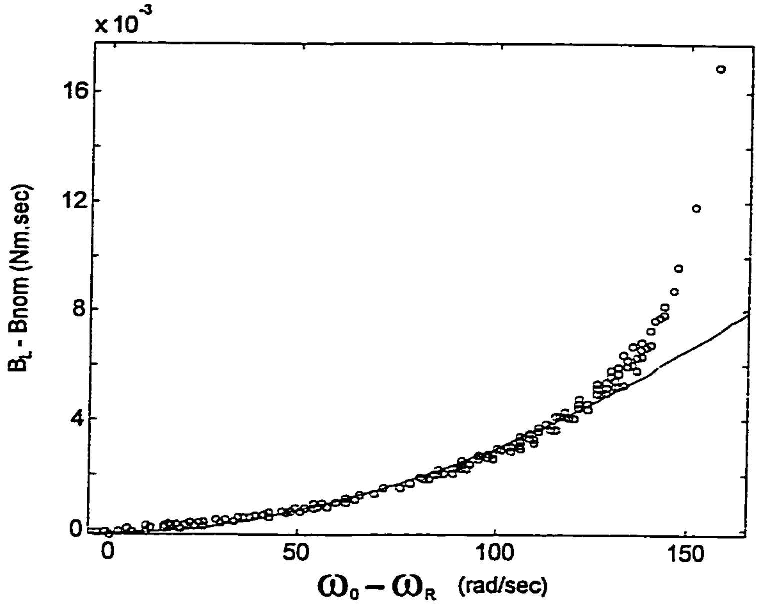

Figure 5..2: Obtaining ΔB_L by fitting a 2 degree polynomial to experimental data

Obtaining J_{Lnom} From Equation (5..4), a step input of i^*_{Sq} would lead to an initial acceleration of $i^*_{Sq} \times Kt/J_L$. The nominal value of J_L can therefore be estimated from such transient trajectories as shown in Figure 5..5. To emphasize stability in the design, J_{Lnom} is chosen to be 0.0071 $Nm.s^2$, the smallest value encountered in normal operation.

Accommodating Tolerances, Unknown and Neglected Dynamics To accommodate deviations from the nominal model, the frequency response of the actual plant can be compared to the nominal plant model. In Figure 5..6, normalized inputs (i^*_{Sq}) and outputs (ω_R) of the feedback linearized plant are shown. The inputs are discrete time sinusoids with a DC offset. The DC offset ensures the compressor will rotate in the

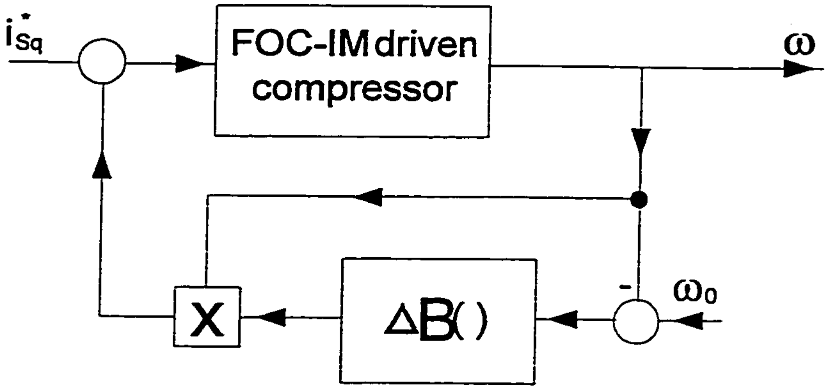

Figure 5..3: Implementation of feedback linearization

correct direction for proper lubrication.

$$i_{Sq}^* = 1.2 + 0.1sin(2\pi fkTs)\,A \quad Ts = 1.5ms \quad k = 0,1,2... \tag{5..6}$$

Data are normalized for making visual comparison of the shape of the output to that of a sinusoid. The rapid fluctuations of ω_R are mainly caused by cyclic variations of J_L with respect to crankshaft angle.

Two features from Figure 5..6 are relevant. Firstly, the shape of ω_R trajectories are very close to being sinusoidal. This fact provides a justification for representing the plant by an LTI model. Secondly, as the amplitude of the output sinusoidal envelop decreases at high frequencies, the uncertainties of both the amplitude and phase response increases.

To accommodate the effect of tolerances in K_t, J_L and B_L, upper and lower bounds of the amplitude response can be generated by substituting suitable combinations of extreme parametric values in Equation (5..4). The neglected and unknown dynamics are assumed to be manifested as deviations of the observed magnitude re-

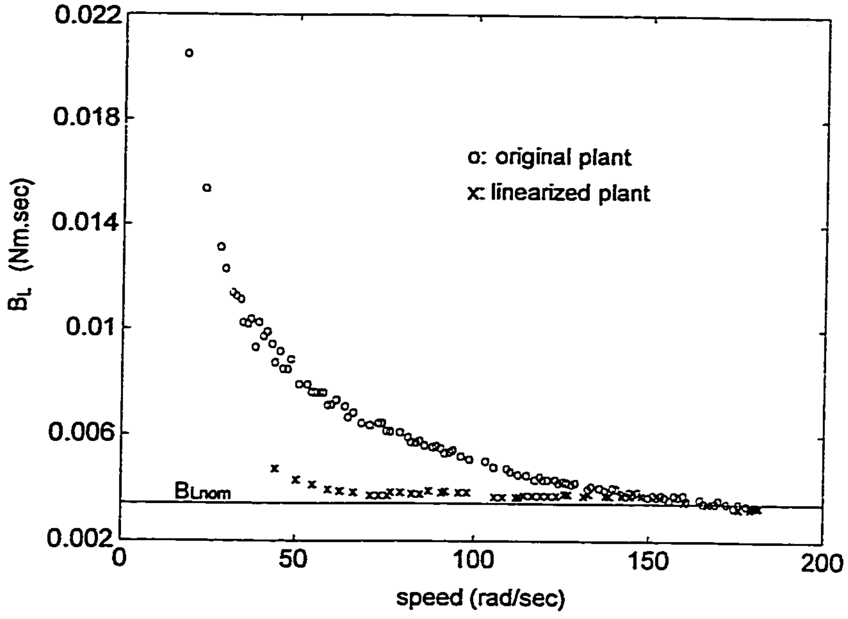

Figure 5..4: Coefficient of friction at various speeds before and after feedback linearization

sponse from that of the nominal model. To represent these effects, simple linear fractional terms of the form $(ap+1)/(bp+1)$ can be incorporated to shape the upper and lower bounds. The following general equation concludes the modelling of the motor-compressor plant.

$$G_x \triangleq \frac{K_{tx}(a_1p+1)(a_2p+1)}{(J_{Lx}p+B_{Lx})(b_1p+1)(b_2p+1)}$$

where x can be any of the subscripts *nom*, *min* or *max*. The corresponding parametric values for G_{nom}, G_{min} and G_{max} are shown in Table 5.1.

The magnitude responses of the nominal plant (G_{nom}) and its bounds (G_{min}, G_{max}) are shown in Figure 5..7.

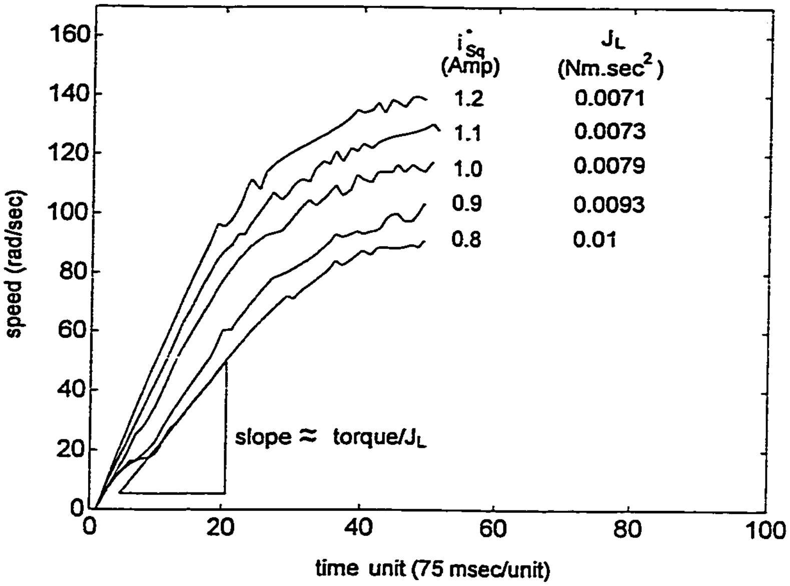

Figure 5..5: Estimation of J_L from transients of step response data

Table 5.1: Parameters for Gnom, Gmin and Gmax

parameters	*nom*	*min*	*max*
K_t	0.47	0.43	0.49
J_L	0.0071	0.006	0.01
B_L	0.002	0.0018	0.005
a_1	0	0	6
a_2	0	0	0.4
b_1	0	0.6	3
b_2	0	0	0.14

5.3 Compensator Design

Characterizing $\tilde{G}$ with $|W_2|$ With the upper and lower boundaries of $\tilde{G}$ defined by G_{ub} and G_{lb}, $|W_2|$ in Equation (4..1) can be obtained as

$$|W_2| = \frac{Max\{|G_{ub} - G_{nom}|, |G_{lb} - G_{nom}|\}}{|G_{nom}|} \tag{5..7}$$

The shape of W2 thus obtained is shown in Figure 5..8.

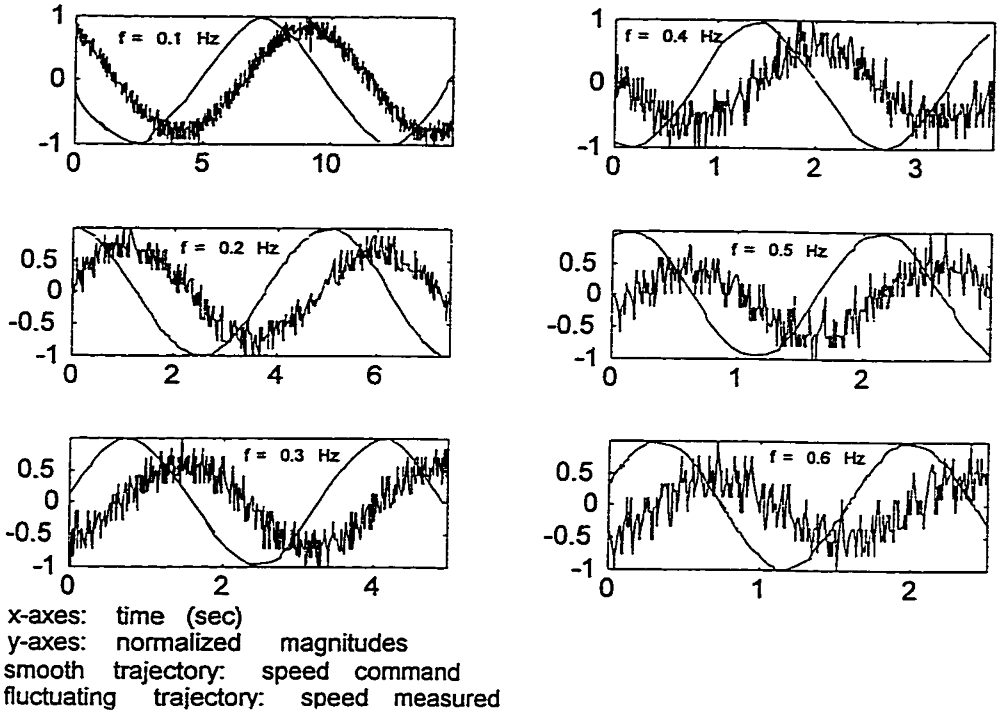

Figure 5..6: Small signal frequency experimental results for model verification

Specifying Performance Requirements by W_1 Command tracking and torque disturbance rejection are two main objectives in the design of a closed loop system. For a compressor, the force acting at the top of a piston has a frequency directly proportional to the compressor speeds (more than $100 rad/s$). The torque disturbance thus produced is usually rejected by installing a massive flywheel on the compressor. The speed controller is therefore required to achieve command tracking in the face of uncertainties. Furthermore, the time domain tracking of a step command should not have any overshoot. This is because a reciprocating compressor must be rotated in a single and correct direction for proper lubrication. If overshoot is allowed, the angular velocity will become negative as an overshoot of the step command from say,

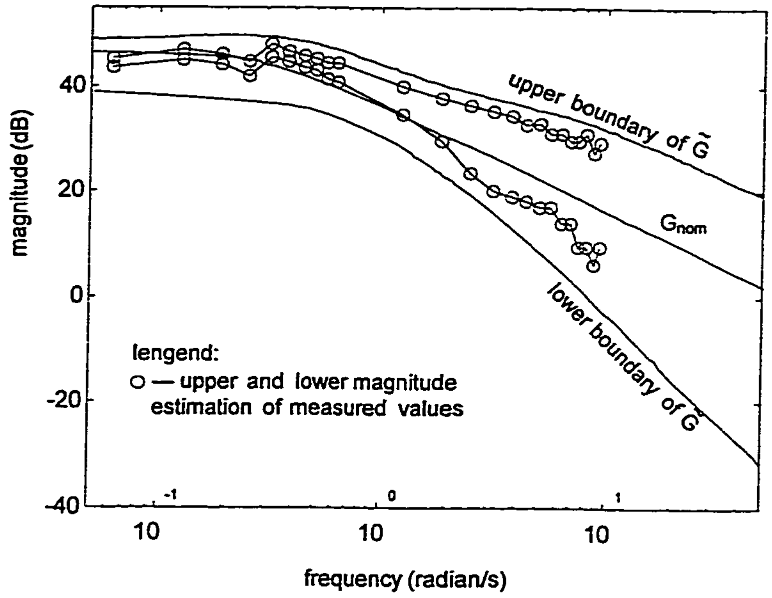

Figure 5..7: Construction of boundaries of $\tilde{G}$ to enclose experimental results

166 *rad/s* to 0 *rad/s*; and damages to the compressor may occur.

For the purpose of emergency speed reduction, it is supposed that the compressor is required to decelerate from rated speed to 10% of rated speed within $T = 10$ seconds. The closed loop bandwidth required is therefore approximately $\frac{\pi}{2\times T} = 0.157$ *rad/s*.. A brick wall LPF with cut off frequency at 0.1*rad/s* with an unspecified DC gain g would be an appropriate representation of W_1 in Equation (4..7). The expected steady state error would be $100/(1+g)$ percent.

$$|W_1| = g, \quad \omega \leq 0.1 \qquad (5..8)$$

The DC gain g is left unspecified because robust stability is of prime concern. The value of g can only be as large as allowed after robust stability is satisfied.

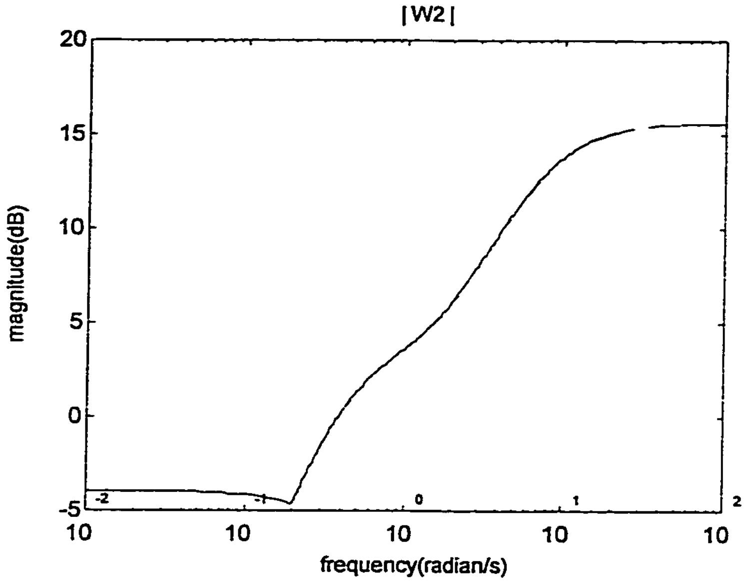

Figure 5..8: Uncertainty in magnitude response

<u>Compensator Design by Loop Shaping</u> A compensator K is constructed so that $|L| < 1/|W_2|$ at high frequencies. After achieving robust stability, the value of g in W_1 is found. By iterating the above processes, the highest value of g achieved is approximately 10 and the resulting *analog* compensator is

$$K = \frac{(s+0.3)(s+0.7)}{(s+0.05)(s+0.08)} \tag{5..9}$$

The shape of the uncompensated plant G_{nom}, $|W_1|$, $1/|W_2|$ and $L \triangleq KG_{nom}$ are shown in Figure 5..9.

The robust stability and robust performance checks are shown in Figure 5..10.

At the top of the figure, the magnitude $|W_2T|$ is plotted. Since the magnitude is less than 0 dB at all frequencies, the robust stability objective is achieved. At high frequencies, $|W_2T|$ is further away from the 0 dB line. Therefore the system should be able to tolerate more deviations than expected in high frequency dynamics. At

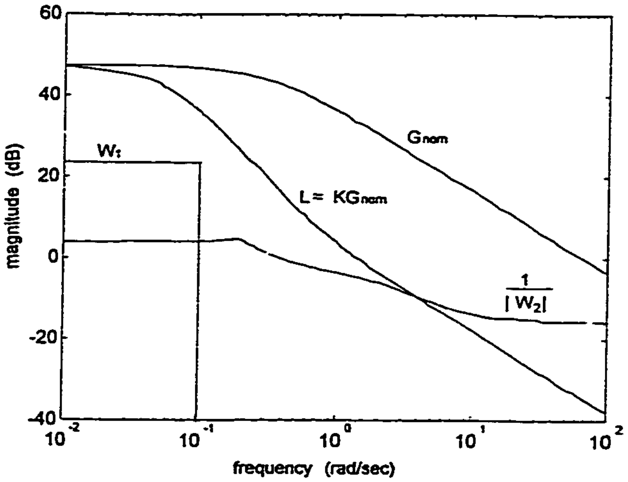

Figure 5..9: Shape of open loop transfer function L

the lower part of the figure, it is clear that $|W_1S| + |W_2T|$ is very close to the $0dB$ line. Therefore the performance described by W_1 cannot be achieved when the true plant is not a member of $\tilde{G}$.

5.4 Implementation of Speed Controller

Choice of sampling interval for speed loop Let

$$K_d \triangleq \begin{bmatrix} A_d & B_d \\ C_d & D_d \end{bmatrix}$$

be the discrete time controller obtained by discretizing the analog speed controller K with a sampling interval h. Let u and u_d be the continuous time input to K and the sampled input to K_d respectively. If h is sufficiently small, the output y_d generated by K_d is expected to be close to the output y generated by K. However, further reduction of h for a system with fast poles would lead to significant truncation errors that could cause the system to become unstable.

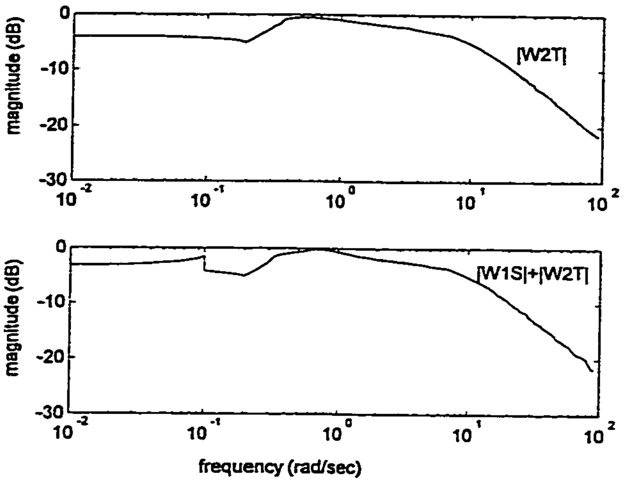

Figure 5..10: Checks for robust stability and performance

Through trial and error, h is determined to be 0.075 seconds, which is 50 times the sampling interval of the field orientation routines. The discretized system with such a sampling period would have gain and phase margins shown in Figure 5..11.

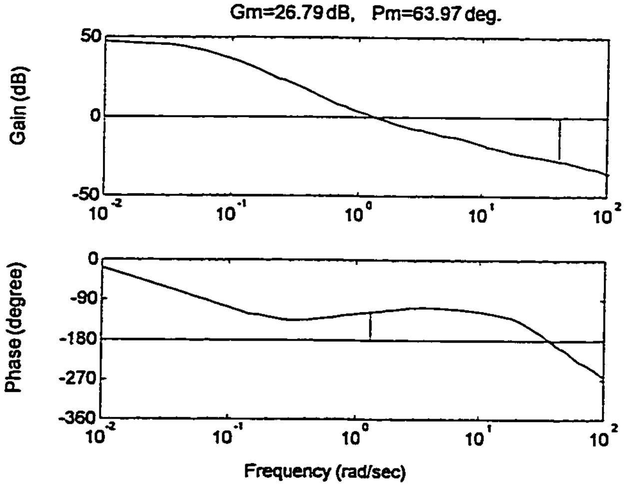

Figure 5..11: Gain and phase margins of compensated system

The bandwidth of the closed loop system can be found from the frequency response of $tf : \omega_R^* \mapsto \omega_R$ shown in Figure 5..12. The closed loop system is expected to track closely commands with frequencies less than or equal to the target 0.157 *rad/s.*, provided the hardware limits are not exceeded at all instances.

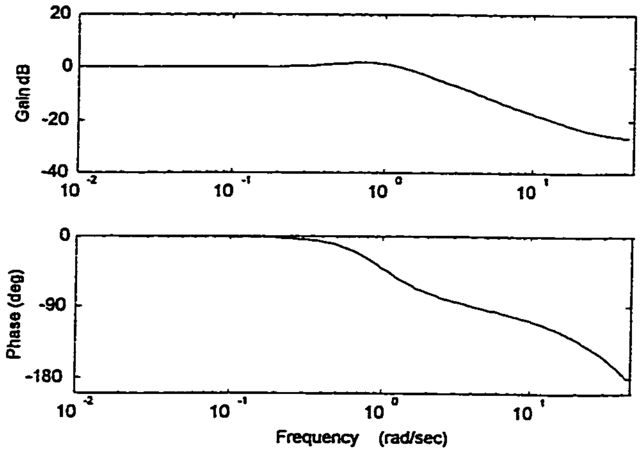

Figure 5..12: Closed loop frequency response

Command filtering To avoid the associated problems of excessively large actuator signals due to large step changes in command, the simplest method is to filter the command by a LPF. To comply with the objective of tracking full command swings within 10 *seconds*, a first order digital LPF with corner frequency at 0.2 *rad/s* can be used for filtering step inputs.

5.5 Results

For most users, the ultimate acceptance criterion is the time domain performance. A thorough verification of robust performance therefore requires conformance of specified performance when the plant is perturbed to its expected extremities. This is not always possible under practical situations due to the nature of the uncertainties, explained as follows.

- Unknown dynamics, the estimate of which is represented by the shape of the upper and lower bound of $\widetilde{G}$ in the frequency domain. The nature of being unknown implies that the plant cannot be made to operate at either the upper or the lower bound.

- J_L is a parameter observed when the plant is treated as if it is of first order. It is believed that J_L is mostly related to the mass of mechanical assemblies and will not change during the life time of the plant. The tolerance of J_L incorporated in the design accommodates unknown dynamics, perhaps due to the influence of friction on acceleration. As a result, the plant cannot be commanded to operate at a given value of J_L.

- B_L is a parameter related to friction and hence is a very complicated function of rotational speed, material conditions and properties of lubricants. For a compressor that is properly maintained and operated below a specified temperature, it is assumed that B_L would be related to rotational speed only. It is possible to manipulate the value of B_L by replacing the lubricating oil in the crankcase. However, this has not been done due to the time constrain of this project.

- K_t can be considered as the DC gain of the motor from the current command i^*_{Sq} to the generated torque T_e. It can be affected by a change of voltage across the DC link of the inverter, which in turn changes the effective magnetizing current i_{Sd}; or by the discrepancies between parameters $[\widehat{R}_S, \widehat{R}_R]$ with the actual resistances $[R_S, R_R]$.

Among the above four conditions, only the last one can be readily tested. The test results are presented next.

Tracking under nominal conditions In Figure 5..13, the trajectories of filtered commands and measured motor speeds are shown. It is clear that the closed loop tracking system performs properly, and the actuator signal u_S/u_{dc} is always less than the hardware limit.

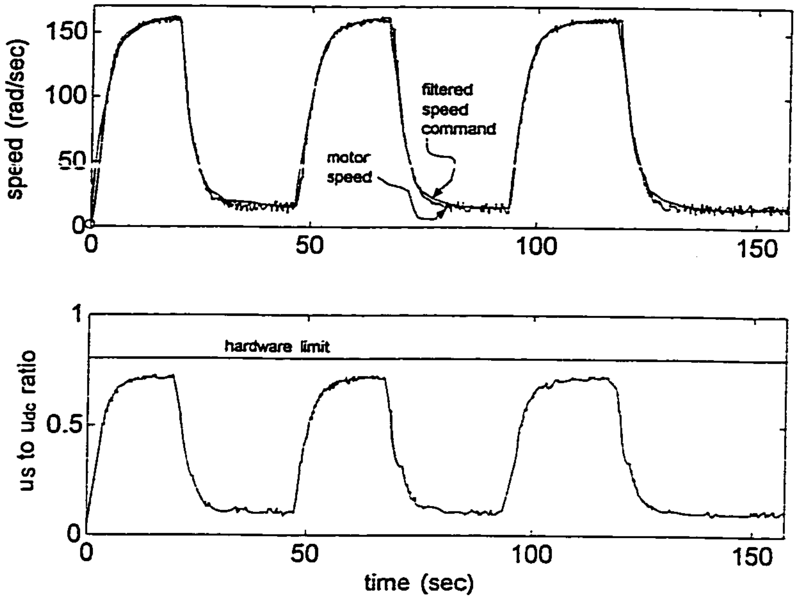

Figure 5..13: Experimental results: speed tracking under nominal conditions

Tracking under reduced magnetizing current For a partial verification, the motor gain K_t can be reduced from its nominal value of 0.47 to the expected minimum of 0.43 by adjusting the magnetizing current i_{Sd}^* by a ratio of 0.43/0.47. The tracking of the filtered command and the size of the actuator signal are shown in Figure 5..14.

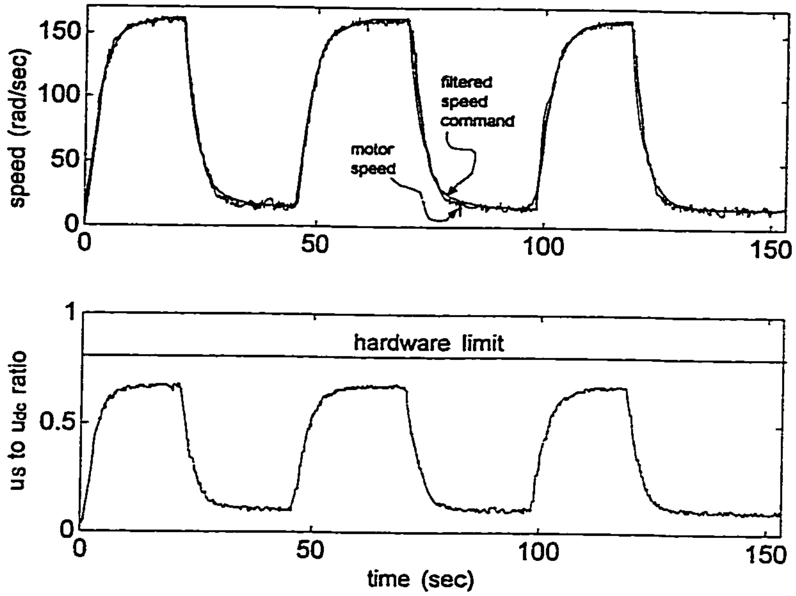

Figure 5..14: Test results on tracking under reduced i_{Sd}^*

Tracking under increased magnetizing current Similarly, the value of K_t being increased to 0.59 can be realized by increasing i_{Sd}^* by a factor of 0.49/0.47. The performance in speed tracking are shown in Figure 5..15.

Tracking under detuned resistance parameters From Figure 3..17, T_e (and hence K_t) would be reduced by a factor of 0.43/0.47 when $[\widehat{R}_S, \widehat{R}_R]$ is reduced by a factor of 0.9. This corresponds to actual resistances $[R_S, R_R]$ being greater than the parameters $[\widehat{R}_S, \widehat{R}_R]$ when the motor warms up. The tracking performance of such a perturbation is shown in Figure 5..16. Since $[\widehat{R}_S, \widehat{R}_R]$ are obtained when the motor is cold, the case of actual resistances being smaller than parameters used in the control program will not be considered.

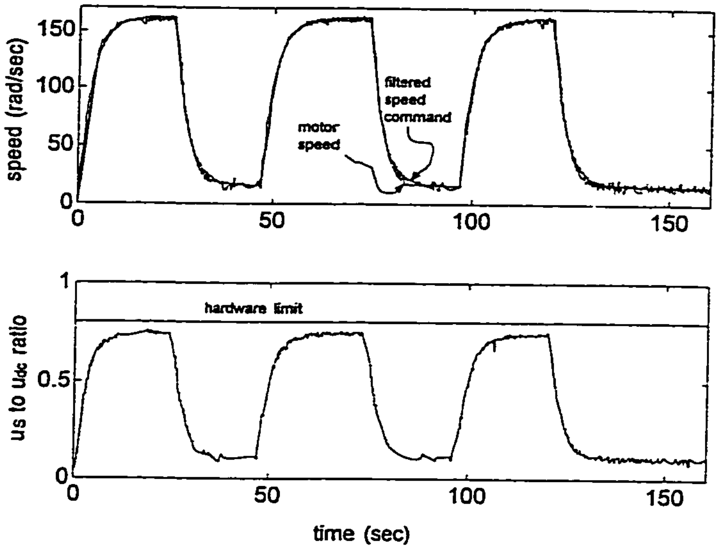

Figure 5..15: Test results on tracking under increased magnetizing current

Interpretation of results All the previous test results showed proper command tracking with actuator signals u_S/u_{dc} less than the hardware limit. Thus **robust performance has been achieved under the tested conditions.** Since under reduced magnetizing current, u_S/u_{dc} has the smallest peak, the nominal magnetizing current should be reduced.

5.6 Discussion

Any one can build a bridge, but the one built by an engineer should satisfy the specifications with minimum resources. It is appropriate to ask whether system components has been overdesigned, and whether the control algorithm has been too conservative.

From Figure 5..15, it can be seen that at steady state, u_S is very close to its

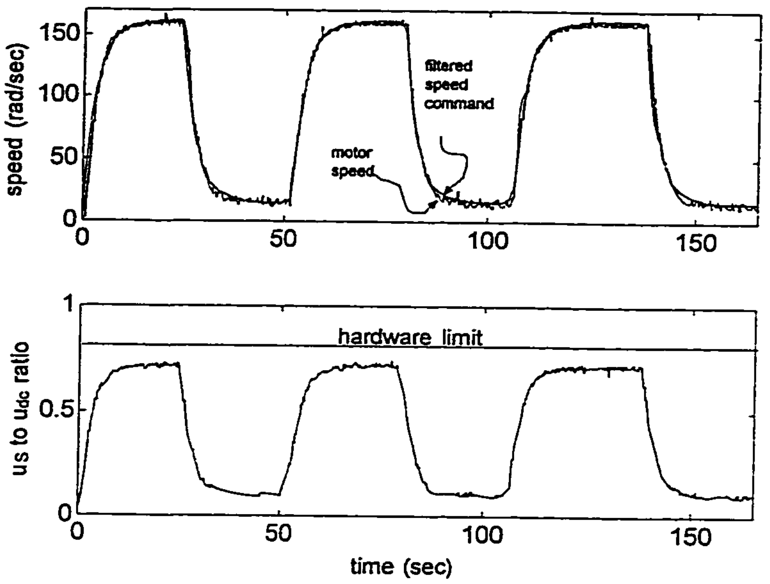

Figure 5..16: Test results on tracking under detuned resistance parameters

limit. From a control system point of view, the available power of the VSI is being efficiently utilized. It should be noticed that at present, the limit on u_S is caused by the ratio of the computation time to the sampling period of the current loop (Section 3.2). That is, the limit is not caused by the current capacity of wires, cables and components.

For faster settling time, a higher order controller may be needed to achieve an underdamped step response. However, there are at least three reasons for not doing so. The first one is because of the closeness of u_S to its limit at steady state. An overshoot during the transient period would lead to violation of the limit and results in damage of the electrical hardware. The second reason is that a compressor must rotate in the correct direction for proper lubrication. An underdamped step response from full speed to zero would cause the compressor to rotate in the wrong direction. The last reason is due to the ignorance of the mechanical strength of the crankshaft and drive belts. Without knowing these properties, it is safe to accelerate the compressor as slow as the application would allow. In fact, it is irrelevant to discuss the conservativeness of the control algorithm without knowing the limits of the strength of the crankshaft and drive belts.

The controller obtained in this project has the form of two lag compensating terms cascaded together. If the design problem is approached in the classical manner with the requirement to satisfy $|W_1S| < 1$, the resulting controller might also be of the same form. However, classical methods do not explicitly incorporate uncertainties in the design procedure, a controller achieving a gain margin of say, 6 dB and phase margin of 30 degree might be considered as being sufficient. Since the deviation of model from the true plant have not been considered in the classical approach, the resulting system may not perform as designed. It is unlikely that a controller designed by classical methods would achieve the same robust performance criterion as the K described in Equation (5..9).

5.7 Summary

A simple LTI model is proposed for the motor-compressor plant. To make the plant conform to such a model, feedback linearization is first applied to modify the plant. From experimental data, the nominal parameters and the perturbed plant set are established. Time domain performance criteria are proposed and approximated by simple frequency domain requirements. Loop shaping is used for constructing a robust speed controller. Verification of robust performance is presented in the frequency domain. The need of a command filter for compliance with design objectives is explained. Finally, various test results are presented for hardware verifications of the system robustness in the time domain.

CHAPTER 6.

CONCLUSIONS AND FUTURE WORK

6.1 Conclusion

The design, implementation and testing of a robust speed controller for a reciprocating compressor coupled to a VSI driven FOC-IM is presented in this thesis. Under the test conditions of detuned motor capacity, the system performs as designed in that 90% of the speed changes for step commands of 0 to 1600 *rpm* (or 1600 to 0 *rpm*) are achieved in less than 10 seconds.

6.2 Recommendations Future Work

Anomaly in the voltage angle of the VSI Under no load conditions ($i_{Sq}^* = 0$), it was found that the voltage angle realized by the VSI can be off target by as much as 12^o electrical when i_{Sd}^* is smaller than 1 A. Preliminary investigations and results are presented in Appendix A6. Further investigation is warranted..

Accuracy and precision in estimating $\hat{i}_{Sd}$ and $\hat{i}_{Sq}$ from line currents It is suggested in Section 2.7 that line currents measured when the inverter is at the zero output state will be 'contaminated' by an unknown portion of i_{Sq}, thus leading to inaccurate estimations of the flux vector. A probable strategy to investigate this phenomena is to compare the results of $\hat{i}_{Sd}$ and $\hat{i}_{Sq}$ derived from line currents at different switching frequencies with constant i_{Sd}^* and i_{Sq}^*.

Detuned operations From investigations in this thesis, the torque trajectories exhibited different behaviors for different direction of detuning. Specifically, for a constant torque command, the actual torque oscillates only when $[R_R, R_S] < [\widehat{R}_R, \widehat{R}_S]$. It would be useful for future references to find out (through simulations) the time trajectory of the discrepancies between estimated and the 'true' flux vector under detuned conditions.

Saturation feedback for varying limits The saturation feedback technique published by [M2] enables better equipment utilization when the hardware limits are constant. It would be interesting to find out if the technique as it is would be suitable for well defined varying limits. A simple introduction to the technique is shown in appendix A7.

Completion of the pressure loop Due to the lack of a pressure sensor and associated data acquisition circuits, the compressor used in this project is arranged to discharge to atmosphere. For completeness, a regulatory pressure loop specification and design should be performed when equipment becomes available.

REFERENCES

[A1] A. Abbondanti,"Method of Flux Control in Induction Motors Driven by Variable Frequency, Variable Voltage Supplies", IEEE/IAS Intl. Semi. Power Conv. Conf., pp.177-184, 1997.

[B1] F. Blaschke, "The Principle of Field Orientation as Applied to the New TRANSVEKTOR Closed-Loop Control System for Rotating Field Machines", Siemens Zeitschrift 1971, pg. 575.

[D1] Doyle J. C., B. A. Francis and A. Tannenbaum, "Feedback Control Theory", Macmillan, New York, 1991.

[G1] R. Gabriel, W. Leonhard and C. Nordby,"Microprocessor Control of Induction Motors Employing Field Coordinates", IEE 2. Int. Conf. on "Electrical Variable-Speed Drives", London, Sept., 1979.

[H1] K. Hasse, "Zum Dynamischen Verhalten der Asynchronmaschine bei Betrieb mit variabler Staenderfrequenz und Staender-spannung" ("On the dynamic behavior of induction machines driven by variable frequency and voltage sources"), ETZ-A Bd 89 H.4, pp.77-81, 1968.

[H2] A. Hughes, J. Corda and D.A. Andrade, "Vector Control of Cage Induction Motors: a Physical Insight", IEE Proc. Electr. Power Appl., Vol. 143, No. 1, January 1996.

[K1] P. Krause, O. Wasynczuk, and S. Sudhoff, "Analysis of Electrical Machinery", IEEE Press, 1995.

[K2] R. J. Kerkman, B. J. Seibel, T. M. Rowan and D. W. Schlegel, "A New Flux and Stator Resistance Identifier for AC Drive Systems", IEEE Trans. Ind. Appl., Vol. 32, No. 3, May/June 1996.

[L1] W. Leonhard, "Control of Electrical Drives", 2nd Edition, Sringer-Verlag Berlin Heidelberg New York, 1996.

[L2] R. Lorenz, T. Lipo, and D. Novotny, "Motion Control with Induction Motors", Proceedings of the IEEE, Vol. 82, no. 8, August 1994.

[L3] F. J. Lin, 'Robust speed -controlled induction-motor drive using EKF and RLS estimators', IEE Proc. Electr. Power Appl, vol. 143, No. 3, May 1996.

[L4] Y.T. Kao and C.H. Liu, "Analysis and Design of Microprocessor-Based Vector-Controlled Induction Motor Drives", IEEE trans. ind. electr. Vol.39. No. 1, Feb, 1992.

[L5] G.-M. Liaw and F.J. Lin, 'A Robust Speed Controller of Induction Motor Drives', IEEE Trans. Industrial Electronics, vol. 41. No. 3, June 1994.

[M1] T. Matsuo and T. A. Lipo, "A rotor Parameter Identification Scheme for Vector-Controlled Induction Motor Drives", IEEE Trans. Ind. Appl. Vol. 1A-21, No. 4, May/June 1985.

[M2] R. H. Middleton, "Dealing with Actuator Saturation", appeared in pp377-381, "The Control Handbook" edited by W. S. Levine, CRC Press Inc., 1996.

[M3] M. Mohamadian, A Thesis, "Indirect Field Oriented Control of an Induction Motor Implemented with an Artificial Neural Network", Department of Electrical and Computer Engineering, 1998.

[T1] D. Tardiff, A Thesis, "Design Considerations for Bipolar Power Transistor Switching Circuits", Department of Electrical Engineering, University of Calgary, 1990.

[T2] Y.-Y. Tzou, 'DSP-Based Robust Control of an AC Induction Servo Drive for Motion Control', IEEE Trans. Control Systems Technology, vol. 4. No. 6, November 1996.

[V1] P. Vas,"Vector Control of AC Machines", Oxford University Press, New York, 1990.

[W1] S. Williamson, R. C. Healey,"Space Vector Representation of Advanced Motor Models for Vector Controlled Induction Motors", IEE Proc.-Electr. Power Appl., Vol 143, No. 1., 1996.

[W2] C. Wang, D. W. Novotny, T. A. Lipo, "An Automated Rotor Time Constant Measurement System for Indirect Field-Oriented Drives", IEEE Trans. Ind. Appl., Vol. 24, No. 1, January/February 1988.

[Z1] K. Zhou, J. Doyle, "Essence of Robust Control", Prentice Hall International Inc., 1997.

APPENDIX A.

INTENDED APPLICATION

Figure A..1 shows a simple line diagram of compressor arrangements at the input of a gas processing plant. Low pressure gas at approximately 20*psig* from the field must be compressed to a pressure of 500*psig* for processing. The overall compression ratio in terms of absolute pressure is approximately 15 : 1. The compression is usually done in two stages. The first stage is commonly performed by reciprocating compressors which would provide a high compression ratio of about 7 : 1; limited by the designed strength of the compressor; and the allowable temperature rise of the compressed gas to avoid explosive hazards in case of leakages. Subsequently, the outputs from various reciprocating compressors in different locations are cooled by intercoolers, and routed to the inlet of a rotary type compressor for compressing to a final pressure of 500*psig* for various processes.

A.1 Benefits in Variable Speed Operation

In a system that involves fluid flow, unmatched flow rates between interconnecting subsystems would invariably lead to a waste of energy in either throttling or recirculating the flow stream. For a gas plant, unmatched flow leads to an additional problem. When the demand of flow from the gas plant is suddenly reduced, constant flow of gas delivered by fixed speed operation of compressors would lead to a pressure rise at the inlet to the gas plant. To prevent damage to equipment, a common practice is to have the excess gas relieved and flared at the top of a stack. The burning of

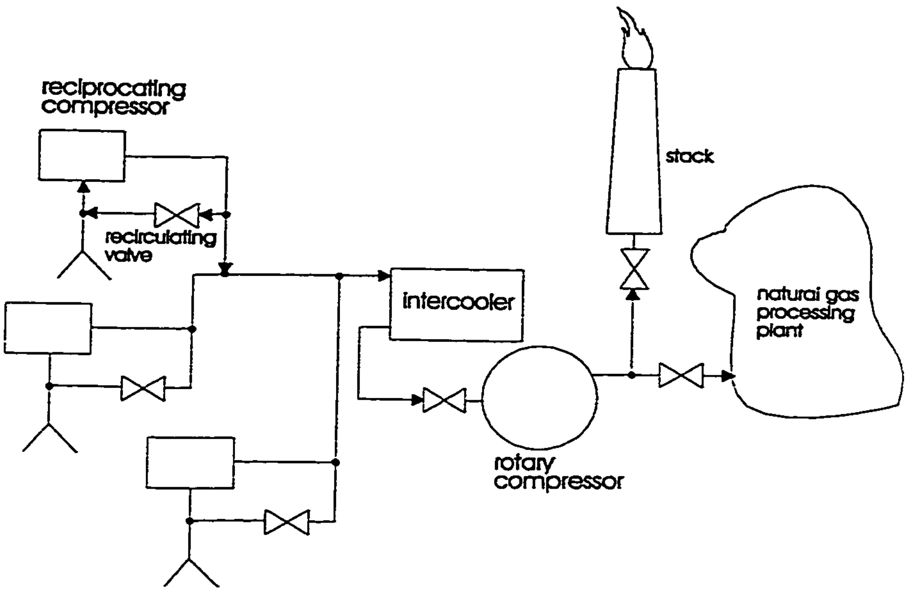

Figure A..1: A typical natural gas compression system

unprocessed natural gas at the stack is an environmental hazard as well as a waste of energy.

A method for avoiding unmatched flow between subsystems is proposed, that is, to employ variable speed drives for the compressors. The conventional drive for an industrial reciprocating gas compressors is the internal combustion engine. Unfortunately, engines must be operated above an idling speed. Various methods such as output recirculation and intake valve unloading are employed to accommodate flow variations with limited successes. In practice, for operations that demand low flow rates, such as start up and emergency shut down, flaring of gas is still a common operating procedure. Recently, the advances in the theory of FOC-IM and electronic hardwares allow a zero to full speed operation of an induction motor in an efficient manner. The advantages of using an induction motor compared to the internal combustion are explained below.

A.2 Benefits of Using an Induction Motor as a Prime Mover

In comparison to an internal combustion engine, an induction motor has the following advantages.

- Low maintenance cost: The auxiliary equipment associated with an electronically controlled induction motor drive are an inverter and a microprocessor. These static electronic equipment seldom fail once they are commissioned. The only routine maintenance required for an induction motor would be the replacement of two easily accessed bearings on the induction motor.
- Reduced start up and shut down time: An induction motor can effectively be started and stopped instantly. To avoid excessive thermal stress, engines above a certain size must be warmed up to above $60^o Celsius$ before starting. This warm up procedure could vary from 2 to $20hrs$. Similarly, the engine must be run at idle for a certain duration before shutting down.
- Full range speed control: The speed of an electronically controlled induction motor can be varied between zero and full speed. Flow demand variations due to fluctuation of operating conditions in the gas process plant can be accommodated easily without resorting to flaring of gas at the stack.
- Reduced pollution: Electricity is mostly generated by the burning of fossile fuel in power plants. In these power plants, various equipment are employed

to control polluting effluents to the environment. For relatively small engines located at a gas well site, such pollotion control facilities are normally not available. Hence using an induction motor to drive a compressor at the well site would lead to less pollutants than using an engine. Moreover, it is generally true that the emission of an engine will only become worse with age; and the auxiliaries associated with an engine often require replenishment of chemicals (such as lubricating oil and glycol).

A.3 Variable Speed Control with an FOC-IM

Previous to the invention of the FOC-IM, the variable frequency control (V/f) was used for providing a continuous speed control for induction motors. The V/f method relies on the change of the synchronous speed to effect a speed change. The amplitudes of terminal voltages are varied in proportion to the frequency in order to avoid exceeding a maximum magnetic flux in the stator. Since the operating principle of the V/f method is based on static torque slip relationships, it does not have direct torque controlling capability. As a result, the torque and hence the speed during transition from one speed to another are difficult to predict and control in the case where a fast torque response is desired.

As the FOC-IM technology matures, more and more industrial applications can benefit from using an FOC-IM as a prime mover. There are many forms of FOC-IM. A common one is to monitor the speed of the rotor and the phase currents. From these monitored variables, a derived variable linearly proportional to the instantaneous electromagnetic torque can be established. Thus a linear input-output model can be obtained for an instantaneous torque control of an induction motor. Using this model as an inner loop allows the speed of the induction motor to be controlled effectively by a linear controller.

A.4 Feasibility Considerations

With the aim of accommodating a operating speed range of zero to full speed, there is an inherent inconvenience associated with low speed, high discharge pressure operations. The thickness of lubricating films on bearing surfaces are directly related to the rotational speed and lubricating oil pressure. For compressors with integral lubricating oil pumps, the oil pressure would drop as the speed is reduced. Prolonged high pressure, low speed operation would therefore cause damage to the bearings. For compressors that are equipped with a separate lubricating oil system, the thickness of the oil films at bearing surfaces can be compensated by employing a higher lubricating oil pressure at low speed.

Another main disadvantage in using electronically controlled induction motors as drives in comparison to gas engines is the requirement of a power supply. The cost associated with procuring a three phase supply at each gas site would depend on existing infrastructures at the gas field. This cost may become justifiable when the restrictions on environmental pollution become more stringent.

APPENDIX B.

SPACE VECTORS

B.1 Construction of Space Vectors from Phase Variables

Space vectors are defined in terms of phase variables. For a three phase, two pole squirrel cage motor with isolated neutral, a space vector $\underline{f}(t)$ is a complex variable constructed from the phase variables $f_A(t)$, $f_B(t)$, and $f_C(t)$.

$$\underline{f}(t) = f_A(t)e^{j0} + f_B(t)e^{j\gamma} + f_C(t)e^{j2\gamma} \qquad \gamma = 2\pi/3 \tag{B.1}$$

The phase variables $f_A(t)$, $f_B(t)$ and $f_C(t)$ can be visualized as the magnitudes of vectors pointing in the directions of the unit vectors e^{j0}, $e^{j\gamma}$ and $e^{j2\gamma}$ respectively. Denoting currents by the symbol i, flux linkages by ψ and voltages by u; and using subscript $_S$ for variables referenced to the stator frame, the three stator space vector variables $\underline{i_S}(t)$, $\underline{\psi_S}(t)$ and $\underline{u_S}(t)$ can be constructed as follows.

$$\underline{i_S}(t) = i_{SA}(t) + i_{SB}(t)e^{j\gamma} + i_{SC}(t)e^{j2\gamma} \tag{B.2}$$

$$\underline{\psi_S}(t) = \psi_{SA}(t) + \psi_{SB}(t)e^{j\gamma} + \psi_{SC}(t)e^{j2\gamma} \tag{B.3}$$

$$\underline{u_S}(t) = u_{SA}(t) + u_{SB}(t)e^{j\gamma} + u_{SC}(t)e^{j2\gamma} \tag{B.4}$$

Similarly, the rotor space vector variables in the *rotor frame* are

$$\underline{i_R}(t) = i_{RA}(t) + i_{RB}(t)e^{j\gamma} + i_{RC}(t)e^{j2\gamma} \tag{B.5}$$

$$\underline{\psi_R}(t) = \psi_{RA}(t) + \psi_{RB}(t)e^{j\gamma} + \psi_{RC}(t)e^{j2\gamma} \tag{B.6}$$

$$\underline{u_R}(t) = u_{RA}(t) + u_{RB}(t)e^{j\gamma} + u_{RC}(t)e^{j2\gamma} \tag{B.7}$$

Denoting the angle between the rotor and the stator frames by $\varepsilon(t)$, a space vector variable defined in the rotor (or stator) frame can be transformed to the stator (or rotor) frame by multiplication with $e^{j\varepsilon(t)}$ (or $e^{-j\varepsilon(t)}$). Consider the space vector $\underline{f}(t)$ in Figure B..1. If defined in the rotor frame, $\underline{f}_R(t) = f(t)ej^{\beta(t)}$. If this same vector is viewed from the stator frame, it would be $\underline{f}_S(t) = f(t)e^{j\alpha(t)} = \underline{f}_R(t)e^{j\varepsilon(t)}$.

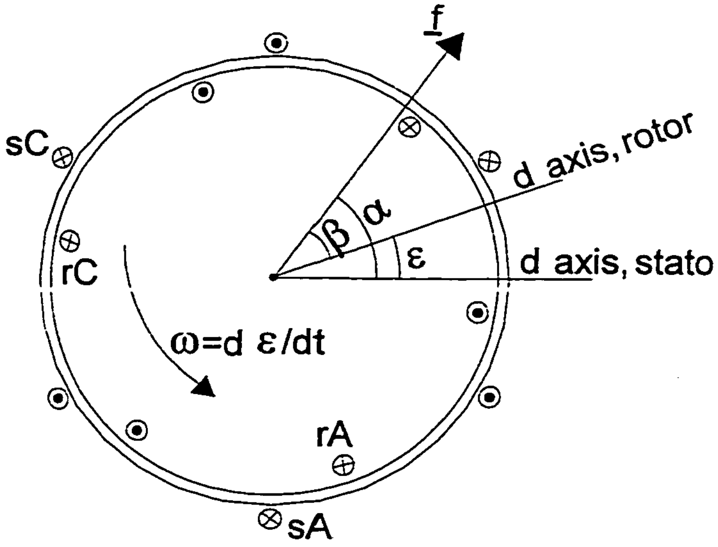

Figure B..1: Space vector and reference frames

B.2 Space Vector Model under Symmetrical Three Phase Supplies

To implement a VSI driven field oriented controlled induction motor, the parameters R_S, R_R, L_S, L_R , L_o,σ_S and σ_R appeared in the model Equations (2..16), (2..17), (2..11), (2..13) and (2..14) must be quantified. In this section, the feasibility of using standard tests to obtain these parameters is established and test results are listed.

When the stator phase to neutral terminals are impressed by an *rms* voltage phasor $\overline{V}_S = V_S e^{j0}$, a corresponding current phasor $\overline{I}_S$ results. The phase voltages and phase currents are

$$u_{sA} = \sqrt{2}V_S\cos(\omega_{syn}t) \qquad u_{sB} = \sqrt{2}V_S\cos(\omega_{syn}t-\gamma) \qquad u_{sC} = \sqrt{2}V_S\cos(\omega_{syn}t-2\gamma)$$

$$i_{sA} = \sqrt{2}I_S\cos(\omega_{syn}t) \qquad i_{sB} = \sqrt{2}I_S\cos(\omega_{syn}t-\gamma) \qquad i_{sC} = \sqrt{2}I_S\cos(\omega_{syn}t-2\gamma)$$

where ω_{syn} is the synchronous speed. Substituting these phase quantities into Equations (B.4) and (B.2), the space vector voltages and currents are

$$\underline{u}_S = \frac{3\sqrt{2}}{2}\overline{V}_S e^{j\omega_{syn}t} \tag{B.8}$$

$$\underline{i}_S = \frac{3\sqrt{2}}{2}\overline{I}_S e^{j\omega_{syn}t} \tag{B.9}$$

The rotor current space vector observed in the rotor frame oscillates with a frequency of $\omega_{slip} = \omega_{syn} - \omega_R$.

$$\underline{i}_R = \frac{3\sqrt{2}}{2}\overline{I}_R e^{j\omega_{slip}t}$$

By introducing these space vector values into Equations (2..3) and (2..4), the following algebraic equations for phasors are obtained.

$$\begin{aligned} \overline{V}_S &= (R_S + j\omega_{syn}\sigma_S L_o)\overline{I}_S + j\omega_{syn}L_o(\overline{I}_S + \overline{I}_R) \qquad (B.10) \\ 0 &= (R_R + j\omega_{slip}\sigma_R L_o)\overline{I}_R + j\omega_{slip}L_o(\overline{I}_S + \overline{I}_R) \end{aligned}$$

Defining slip by $S \triangleq \omega_{slip}/\omega_{syn}$, the rotor voltage equation for phasor can be normalized to

$$0 = (\frac{R_R}{S} + j\omega_{syn}\sigma_R L_o)\overline{I}_R + j\omega_{syn}L_o(\overline{I}_S + \overline{I}_R) \tag{B.11}$$

Equations (B.10) and (B.11) lead to the same single phase equivalent circuit as that obtained from AC analysis shown in Figure B..2.

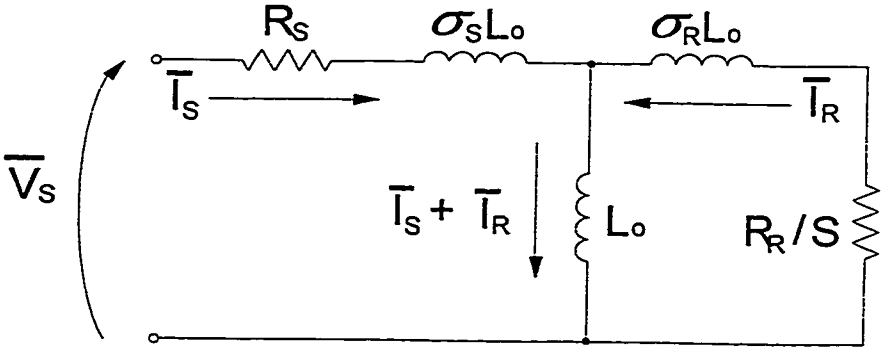

Figure B..2: Equivalent circuit for symmetrical three phase operation

This implies the parameters R_S, R_R, L_o, σ_S, σ_R, L_S and L_R can be obtained by the well known DC, open circuit and locked rotor tests. The parameters thus obtained are listed in Table B.1.

Table B.1: Motor parameters

primary parameter	values	derived parameters	values
R_S	6.085 Ω	L_S	0.3099 H
R_R	4.377 Ω	L_R	0.3161 H
L_o	0.2974 H	σ_S	0.042
L_{LS}	0.0125 H	σ_R	0.0629
L_{LR}	0.0187 H	σ	0.0971

APPENDIX C.

SIMULATIONS FOR A DETUNED VSI DRIVEN FOC-IM

This simulation requires the ode45.m that is included in the student's edition of MatLab. The following two files, vsifoc2.m and vsi.m are written by the author.

```
%%%%%%%%%%%%%%%%%%%%%%%%%%%%%%%%%%%%
%% fileName: vsifoc2.m
%% Written by: Alfred Chu
%% - Simulate torque transients of a detuned VSI driven FOC motor
%% when input is a step command in isqCmd.
%% - Assumes wR is correctly sensed by speed senor. Thus avoids
%% the need for J and B parameters of motor and reduces the
%% complexity of simulation. In the following codes, wR is used
%% as a place holder to show equation but is always set to 0.
%% Dependencies:
%% existence of file vsi.m written by Alfred Chu
%% existence of ode45.m from toolbox of MATLAB
%% Suggestion:
%% Change TOLERANCE to find difference due to 'wrong' resistances.
%% Change NUM to extend duration of simulation
%% Change SIMFACT for different time resolutions used in ode45.m
clear;
%% globals are accessed by ode45 routine
global usd; % d axis voltage, stator referenced
global usq; % q axis voltage, stator referenced
global wmR; % flux speed, stator referenced
global RS;
global LS;
global SIGMA;
global TR;
%% motor parameters
LLS = 0.0125; % stator leakage inductance
R_SENSE = 0.66; % current sensor resistance
RS = 5.425 + R_SENSE; % total stator resistance
RR = 4.377; % rotor resistance
LM = 0.2974; % mutual inductance
LEAK_TOTAL = 0.0312; % -total leakage resistance, note that all other
% inductance related parameters are defined
% by LM, LEAK_TOTAL and LLS.
LLR = LEAK_TOTAL-LLS; % rotor leakage inductance
LS = LM + LLS; % stator inductance
```

```
LR = LM + LLR; % rotor inductance
SIGMA_S = LS/LM-1; % stator leakage factor
SIGMA_R = LR/LM-1; % rotor leakage factor
SIGMA = 1 - 1/((1+SIGMA_S)*(1+SIGMA_R)); % total leakage factor
LSPRIME = SIGMA*LS; % stator subtransient inductance
TR = LR/RR; % rotor time constant
TS = LS/RS; % stator time constant
TSPRIME = LSPRIME/RS; % stator subtransient time constant
NUM_POLE = 4; % number of poles
%% - Identifiers with keyword HAT are used for simulating wrongful
%% parameters and estimations.
%% - The parameters used in control software may be different from actual
%% values. For resistive parameters that were set when motor is cold,
%% their values will always be less than actual resistances when the
%% motor is loaded. Therefore the tolerances should be negative.
TOLERANCE = -50;
RRHAT = RR*(1+TOLERANCE/100);
RSHAT = RS*(1+TOLERANCE/100);
TRHAT = LR/RRHAT;
TSHAT = LS/RSHAT;
TSPRIMEHAT = LSPRIME/RSHAT;
%% FOC operating point
KT = (NUM_POLE/2)*(2/3)*(LM/(1+SIGMA_R));
isdCmd = 1.26; % constant isd command value
slipHatConst = 1/(TRHAT*isdCmd); % reflects method used in FOC control.
isqCmdNormal = 1.26; % - torque = KT*imR*isq, and imR would be
% the same as isdCmd if field orientation is
% correct. It was thought that when isqCmd is
% set to the same value of isdCmd, then detune
% conditions would always cause a reduction
% in torque. It turns out such prediction is
% correct only for a CSI drive. Results on
% VSI drive is quite interesting.
%% Simulation conditions
TSAMP = 0.0015; % 1.5 ms, used in control software.
FLUX_TIME = 500*TSAMP; % reflects flux charging at start up
NUM = 800; % number of TSAMP multiples
TFINAL = NUM*TSAMP; % time to end simulation.
SIMFACT = 5; % for chopping TSAMP into SIMFACT parts
TSIM = TSAMP/SIMFACT; % used in ode45 subroutine, a MATLAB func-
tion
NUM_SAMPLE = NUM*SIMFACT; % number of samples returned by ode45.m
dataSet = zeros(NUM_SAMPLE+1,5); % allocate memories for data
```

```
%% Initialize variables
wR = 0; % rotor speed
wmR = 0; % flux speed
fluxAngleHat = 0; % wrongful est. of flux angle due to wrong paras.
fluxAngle = 0; % the true flux angle
isdqImrOld = [0,0,0]'; % colume vector: [isd[k-1], isq[k-1], imR[k-1]]'
k=1; % index variable
for time = 0:TSIM:TFINAL; % step through time resolution in ode45.m
time % echo time on screen
if (time < FLUX_TIME) % charge flux for FLUX_TIME
isqCmd = 0;
else
isqCmd = isqCmdNormal;
end;
%% At the beginning of every TSAMP, flux speed and position are
%% updated in the FOC control routine as follows.
if rem(time,TSAMP) < 1e-7;
wmrHat = isqCmd*slipHatConst+wR;
fluxAngleHat = fluxAngleHat+wmrHat*TSAMP;
end;
%% The true angle, follows a different trajectory
fluxAngle = fluxAngle+wmR*TSIM;
angDiff = fluxAngleHat-fluxAngle;
%% usdCmd and usqCmd for a VSI driven FOC are calculated as follows
%% in the FOC control routine.
usdCmd = isdCmd*RSHAT-SIGMA*LS*wmrHat*isqCmd;
usqCmd = isqCmd*RSHAT+LS*wmrHat*isdCmd;
usCmd = sqrt(usdCmd*usdCmd+usqCmd*usqCmd);
voltAngHat = atan2(usqCmd,usdCmd);
%% The actual voltage angle imposed on the motor would be different
%% from what we thought in the FOC control routine.
voltAng = angDiff+voltAngHat;
while voltAng > 2*pi;
voltAng = voltAng-2*pi;
end;
while voltAng < -2*pi;
voltAng = voltAng+2*pi;
end;
%% Thus the actual dq axis voltage imposed on the motor is different
%% from the command value.
usd = usCmd*cos(voltAng);
usq = usCmd*sin(voltAng);
%% Calling ode45.m of MATLAB. Analysis effect of usd and usq
```

```
%% according to vsi.m.
[t,isdqImrNew] = ode45('vsi',0,TSIM,isdqImrOld);
isdqImrOld = isdqImrNew(size(isdqImrNew,1),:)';
%% The true slip speed varies with imR rather than isd.
wmR = isdqImrOld(2)/(TR*isdqImrOld(3))+wR;
Te = KT*isdqImrOld(2)*isdqImrOld(3); % Te = KT*isq*imR.
%% Collect data: [time, isd, isq, imR, Te]
dataSet(k,:) =[time,isdqImrOld',Te];
k = k+1;
end;
%%%%%%%%%%%%%%%%%%%%%%%%%%%%%%%%%%%%%%%%%%%%%%%%%%%%%%%%%%%%%%%%%%%%
function isdqmp = vsi(t,isdqm);
%% fileName: vsi.m
%% Written by: Alfred Chu
%% - function used for updating isd, isq and imR using
%% equations published in the book by Peter Vas. This
%% function is called in vsifocx.m indirectly through
%% ode45.m. ode45.m is a function provided in toolbox
%% of MATLAB.
%% - Input variables:
%% t = time duration for simulation
%% isdqm: colume vector holding isd, isq and imR.
%% - Returned variable:
%% isdqmp: vector holding updated isd,isq and imR.
%% globals are defined in vsifocx.m where x is a version
%% number.
global usd;
global usq;
global wmR;
global RS; % stator resistance = 6.0850;
global LS; % stator inductance = 0.3099;
global SIGMA; % overall leakage factor = 0.0971;
global TR; % rotor time constant = 0.0722;
[rows,cols] = size(isdqm);
isdqmp = zeros(rows,cols);
%% update the true isd, isq, imR values according to
%% VSI driven FOC rules (shown in book by Vas)
temp1 = isdqm(1)*RS;
temp2 = SIGMA*LS*wmR*isdqm(2);
temp3 = (isdqm(1)-isdqm(3))*(1-SIGMA)*LS/TR;
isdqmp(1) = (usd-temp1+temp2-temp3)/(SIGMA*LS);
temp1 = isdqm(2)*RS;
temp2 = SIGMA*LS*wmR*isdqm(1);
```

```
temp3 = (1-SIGMA)*LS*wmR*isdqm(3);
isdqmp(2)= (usq-temp1-temp2-temp3)/(SIGMA*LS);
isdqmp(3)= (isdqm(1)-isdqm(3))/TR;

%%%%%%%%%%%%%%%%%%%%%%%%%%%%%%%%%%%%%%%%
```

APPENDIX D.

SIMULATIONS FOR A DETUNED CSI DRIVEN FOC-IM

For comparison, the torque trajectories of a CSI driven FOC-IM under detuned conditions are shown in Figure D..1. Similar to a VSI driven machine, T_e would oscillates when $R_R < \widehat{R}_R$. However, for a CSI driven FOC-IM, the steady state maximum of T_e occurs when $\hat{R}_R$ matches R_R.

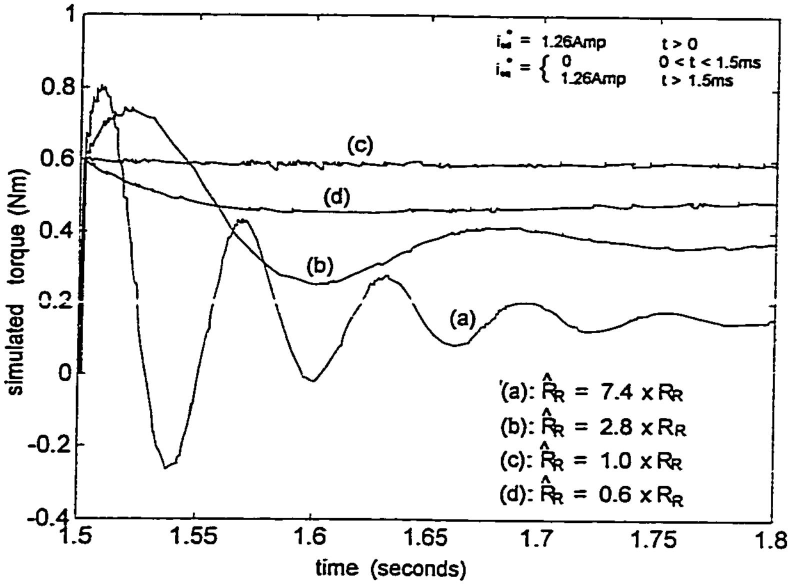

Figure D..1: Simulation of detuned performance of CSI driven FOC-IM

The stand alone MatLab codes for simulating the detuned behaviors of the CSI driven FOC-IM are shown below.

```
%% fileName: csifoc.m
%% Written by: Alfred Chu
%% - Simulates the effect of detuned rotor resistances for a
%% CSI driven FOC-IM
%% Assumption: Rotor position and speed is known accurately
%% at all instances. Thus avoid the need to know
%% Jmotor and Bmotor for the simulation.
clear;
```

```
R_SENSE = 0.66; % current sensor resistance
RS = 5.425 + R_SENSE; % total stator resistance
RR = 4.377; % rotor resistance
LM = 0.2974; % mutual inductance
LEAK_TOTAL = 0.0312; % total leakage inductance
LLS = 0.0125; % stator leakage inductance
LLR = LEAK_TOTAL - LLS; % rotor leakage inductance
LS = LM + LLS; % stator self inductance
LR = LM + LLR; % rotor self inductance
SIGMA_S = LS/LM-1; % stator leakage factor
SIGMA_R = LR/LM-1; % rotor leakage factor
SIGMA = 1 - 1/((1+SIGMA_S)*(1+SIGMA_R)); % overall leakage factor
LSPRIME = SIGMA*LS; % stator subtransient inductance
TR = LR/RR; % rotor time constant
TS = LS/RS; % stator time constant
TSPRIME = LSPRIME/RS; % stator subtransient time constant
%% - Setting isdCmd and isqCmd to the same value implies change
%% of actual values due to detuned conditions will always have
%% a smaller electromagnetic torque for a CSI drive ?
isdCmd = 1.26; % d axis command, flux frame referenced
isqCmd = 1.26; % q axis command, flux frame referenced
isCmd = sqrt(isdCmd*isdCmd+isqCmd*isqCmd);
torqueConst = (4/3)*LM/(1+SIGMA_R); % for a 4 pole machine
thetaCmd = pi/4; % because isdCmd=isqCmd;
TSAMP=0.0015; % sampling period
factor = 10; % chop up a sampling period
smallT=TSAMP/factor; % into 10 parts for analysis
RRHAT = [2.337,4.337,12.337,32.377];% simulates wrongful estimates
for k=1:4;
Te = [0];
angDiff = 0;
time = 0;
timer = [0];
imR = isdCmd; % Assume flux is already established.
alpha = thetaCmd; % At t=0, you cannot be wrong on flux angle.
TRHAT = LR/RRHAT(k); % Simulates wrongful estimate of time constant
slipHat = 1/TRHAT; % and therefore wrong slip speed.
count = factor;
slipAngHat = 0;
slipAng = 0;
while time < 0.3; % Simulate for 0.3 second;
isd = isCmd*cos(alpha);
if time < 0.0015;
```

```
isq = 0; % Charge flux for one more sampling period
else
isq = isCmd*sin(alpha); % true isq
slip = isq/(TR*abs(imR)); % true slip
slipAng = slipAng+slip*smallT; % true slip angle
if count == factor; % do wrong estimate once/Tsamp
slipAngHat = slipAngHat+slipHat*smallT*factor;
count = 0;
end;
count = count+1;
angDiff = slipAngHat - slipAng; % difference between true and wrong
alpha = angDiff+thetaCmd; % this is the actual angle imposed
while alpha > 2*pi;
alpha = alpha-2*pi;
end;
while alpha < -2*pi;
alpha = alpha+2*pi;
end;
end;
Te = [Te,isq*imR*torqueConst]; % Collects the torque data
timer = [timer, time];
y = imR+(isd-imR)*smallT/TR; % because TR*d(imR)/dt + imR = isd
imR = y;
time = time + smallT;
end;
timer = timer+1.5*ones(1,size(timer,2));
plot(timer,Te,'w'); % shift time axis to show relevant portion
hold on;
end;
```

APPENDIX E.

ACCURACY OF VECTOR ANGLE AT NO LOAD

In a series of experiments, the inverter is commanded to impress a stator voltage vector of constant magnitude u_S^* at various angles θ^*. At each of the angles, more than a second is allowed for the line currents to reach their steady state so that the torque producing current i_{Sq} became zero and $i_{Sd} = u_S/R_S$. From line currents measured at steady states, the value of the voltage angle θ that would result in a zero magnitude of i_{Sq} is computed. In Figure E..1a, the angle computed from current measurements (θ) is plotted against the angle command (θ^*) when the steady state magnetizing current i_{Sd} is equal to the rated value. It can be seen that there are patterned discrepancies at various angles. The worst deviation of θ from θ^*, approximately 8 degrees electrical, occurred at angles at multiples of 60 degrees. Attempts in shifting the instance of sampling did not rectify the anomaly. However, when i_{Sd} is reduced, the discrepancies between θ and θ^* are increased as shown in Figure E..1b. The apparent cause of the discrepancies is an unbalanced three phase circuit. This is verified by inspecting the line currents when the vector is at an angle of 0 degree. It is found that i_b and i_c, instead of being equal, were -0.97 and -0.55 A respectively.

Intuitively, the errors shown in Figure E..1 could lead to a torque pulsation if constant torque is being commanded. If the motor is operated at high speed, the effect of this torque pulsation on speed would be masked by the kinetic energy stored in the flywheel of the combined motor and load. The worst case occurs at low speed

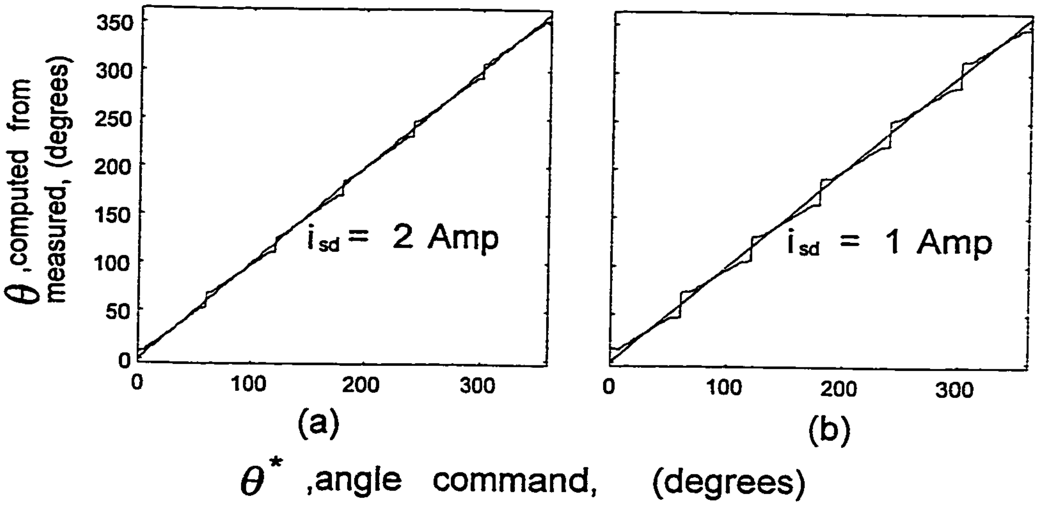

Figure E..1: Experimental results showing non-ideal mapping of flux angles and low load when the realized vector angle deviates most from its command value.

APPENDIX F.

SATURATION FEEDBACK

A speed controller C with numerator and denominator polynomials equal to N_c and D_c respectively, can be modified to a input filtering part and a signal recovery part through positive feedback as shown in Figure F..1.

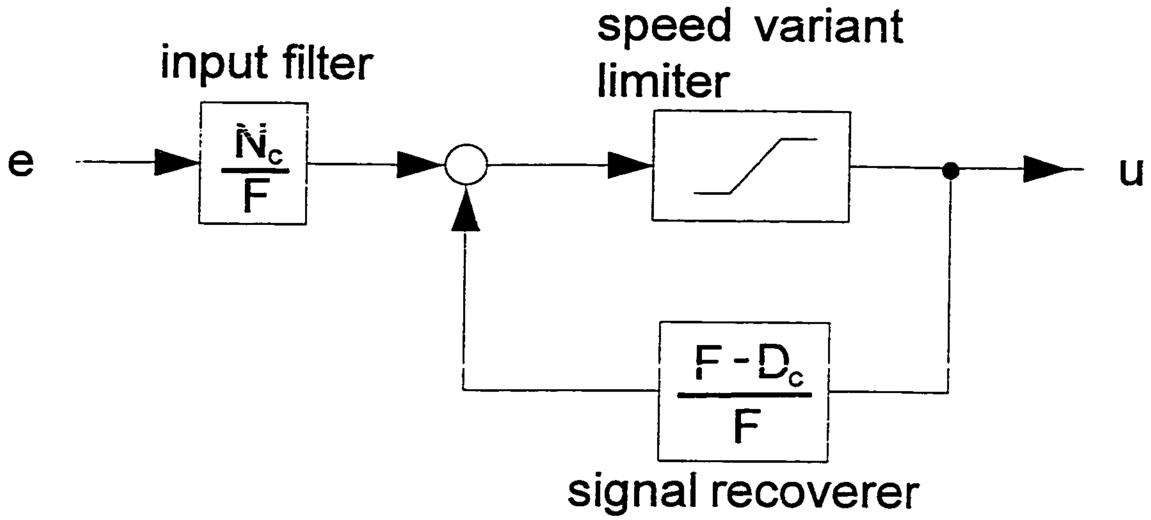

Figure F..1: Saturation feedback to alleviate integrator windup

When the saturation limit is not violated, the positive feedback enables full recovery of the signal u. This can be seen by the transfer function $tf : e \mapsto u = N_c/D_c$ when the gain of the limiter is 1, or equivalently, no saturation has occurred.. When saturation occurs, the gain across the limiter would be smaller than 1 and the size of u is reduced accordingly. Intuitively, if C has any factor p in its denominator, (i.e. C has an integrator), the particular p operator would be moved to the signal recovery part in Figure F..1. When saturation occurs, the time integrating action on e would be reduced. The polynomial F can be viewed as a tuning parameter. It is suggested in [M2] that F should be constructed with the fastest closed loop pole of the original closed loop system.